



**ARTIFICIAL INHOMOGENEOUS  
TAPERED IMPEDANCE SHEET  
CHARACTERIZATION AND APPLICATIONS**

**THESIS**

Jeffrey P. Massman, Lieutenant, USAF  
AFIT/GE/ENG/10-16

**DEPARTMENT OF THE AIR FORCE  
AIR UNIVERSITY**

**AIR FORCE INSTITUTE OF TECHNOLOGY**

**Wright-Patterson Air Force Base, Ohio**

**APPROVED FOR PUBLIC RELEASE; DISTRIBUTION UNLIMITED.**

The views expressed in this thesis are those of the author and do not reflect the official policy or position of the United States Air Force, Department of Defense, or the United States Government.

ARTIFICIAL INHOMOGENEOUS TAPERED IMPEDANCE SHEET  
CHARACTERIZATION AND APPLICATIONS

THESIS

Presented to the Faculty  
Department of Electrical and Computer Engineering  
Graduate School of Engineering and Management  
Air Force Institute of Technology  
Air University  
Air Education and Training Command  
in Partial Fulfillment of the Requirements for the  
Degree of Master of Science in Electrical Engineering

Jeffrey P. Massman, BSEE

Lieutenant, USAF

March 2010

APPROVED FOR PUBLIC RELEASE; DISTRIBUTION UNLIMITED.

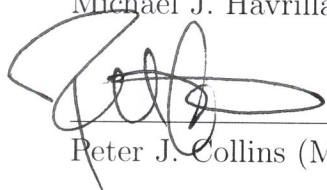
ARTIFICIAL INHOMOGENEOUS TAPERED IMPEDANCE SHEET  
CHARACTERIZATION AND APPLICATIONS

Jeffrey P. Massman, BSEE  
Lieutenant, USAF

Approved:

Michael Havrilla

Michael J. Havrilla (Chairman)



Peter J. Collins (Member)

Andrew J. Terzuoli

Andrew J. Terzuoli (Member)

09 Mar 2010

Date

9 MAR 2010

Date

9 Mar 2010

Date

## Abstract

The ability to manipulate a complex impedance sheet about a PEC or general dielectric cylinder of arbitrary diameter to control the overall scattering characteristics at particular angles for shielding or scattering applications is presented. It is shown that with the capability to readily control both the real and imaginary components of a percolated lossy film's effective impedance, specific impedance distributions can be obtained to effectively direct the overall nulls in the bistatic scattering pattern. The exact approach only requires negligible truncation error of the matrix solution and can be applied to cylinders of arbitrary size. This approach relies on general impedance sheet boundary conditions in addition to a Fourier series representation of the impedance sheet distribution, with the utilization of Wronskian and recurrence relations, to produce a computationally efficient matrix solution for the scattered field expansion coefficient  $a_n$ . This scattering coefficient  $a_n$  can then be included in the expression for a two-dimensional scattering width, allowing for the computation of scattering patterns of arbitrary diameter cylinder impedance sheet distributions. The ability to adapt sheet impedances to effectively control the overall nulls in the bistatic scattering pattern will be demonstrated, with practically-implemented impedance characteristics. Lastly, a novel rectangular X-band waveguide system will be utilized to characterize the electromagnetic properties of the  $\phi$ -dependent impedance sheet.

## Acknowledgements

I would like to express my deepest appreciation to my advisor Dr. Michael Havrilla. His patient mentorship and attention to uncommon physical insight beyond the mathematics has inspired and enlightened me like none before.

Also, I would like to express my gratitude to my family for their love and support through my studies.

Jeffrey P. Massman

## Table of Contents

	Page
Abstract .....	iv
Acknowledgements .....	v
List of Figures .....	viii
List of Tables .....	xi
I. Introduction .....	1
1.1 Problem Statement .....	1
1.2 Limitations .....	3
1.3 Scope .....	3
1.4 Thesis Organization .....	4
II. Background Electromagnetic Theory .....	5
2.1 Constitutive Parameters and Relations .....	5
2.2 Time-Harmonic Electromagnetic Fields .....	6
2.2.1 Boundary Conditions .....	7
2.3 Scattering by Cylinders .....	12
2.3.1 Electromagnetic Scattering Methodologies .....	12
2.3.2 Wave Decoupling due to z-invariance .....	13
2.4 Cylindrical Wave Transformations and Theorems .....	15
2.4.1 $TM^z$ Polarization Development .....	18
2.4.2 $TE^z$ Polarization Development .....	19
III. Analytical Methodology .....	22
3.1 Sheet Impedance Distribution Formulation .....	22
3.2 Free-space Filled Tapered Cylindrical Impedance Sheet .....	26
3.2.1 $TM^z$ Polarization Development .....	27
3.2.2 $TE^z$ Polarization Development .....	34
3.3 PEC Filled Tapered Cylindrical Impedance Sheet .....	40
3.3.1 $TM^z$ Polarization Development .....	41
3.3.2 $TE^z$ Polarization Development .....	43
3.4 Dielectric Filled Tapered Cylindrical Impedance Sheet .....	47
3.4.1 $TM^z$ Polarization Development .....	48
3.4.2 $TE^z$ Polarization Development .....	51

	Page
IV. Experimental Results .....	55
4.1 Bistatic Scattering .....	55
4.1.1 Dielectric pedestal results .....	56
4.1.2 PEC pedestal results .....	60
4.2 Electromagnetic Characterization Process .....	64
4.2.1 Experimental Setup .....	66
4.2.2 0.1 inch Aperture Flange .....	67
4.2.3 0.2 inch Aperture Flange .....	70
4.2.4 0.3 inch Aperture Flange .....	74
4.2.5 Summary .....	78
V. Conclusions and Recommendations .....	80
5.1 Conclusions .....	80
5.2 Future Research .....	80
A. Computationally-Efficient Formulation .....	82
B. Wronskian and Recurrence Relations .....	84
Bibliography .....	87

## List of Figures

Figure	Page
1. Experimental setup variations of the full X-band plates, stepped aperture plates of 0.1, 0.2, 0.3 inches, and stepped aperture sheets of 0.1, 0.2, 0.3 inches. ....	2
2. Impedance sheet boundary condition setup. ....	7
3. High contrast electric field at the impedance boundary. ....	9
4. Impedance sheet boundary condition circuit analogy. ....	11
5. 2D z-invariance physical structure. ....	13
6. Side and top view of bistatic scattering from a cylinder comprised of a $\phi$ -dependent impedance sheet. ....	26
7. Side and top view of bistatic scattering from a cylinder comprised of a $\phi$ -dependent impedance sheet wrapped about a PEC pedestal. ....	40
8. Side and top view of bistatic scattering from a cylinder comprised of a $\phi$ -dependent impedance sheet wrapped about a dielectric pedestal. ....	47
9. Single sinusoid $\phi$ -dependent impedance sheet distribution. ....	57
10. 2D Bistatic Scattering Width of $TM^z$ polarization (Top: 0 degrees, Middle: 23.4 degrees, Bottom: 90 degrees) for the $\phi$ -dependent impedance sheet filled with a polystyrene pedestal. ....	58
11. 2D Bistatic Scattering Width of $TE^z$ polarization (Top: 0 degrees, Middle: 90 degrees, Bottom: 104.4 degrees) for the $\phi$ -dependent impedance sheet filled with a polystyrene pedestal. ....	59
12. 2D Bistatic Scattering Width of $TM^z$ polarization (Top: 0 degrees, Middle: 36.0 degrees, Bottom: 108.0 degrees) for the $\phi$ -dependent impedance sheet partially filled with a PEC pedestal. ....	61

Figure	Page
13. 2D Bistatic Scattering Width of $TE^z$ polarization (Top: 0 degrees, Middle: 90 degrees, Bottom: 104.4 degrees) for the $\phi$ -dependent impedance sheet partially filled with a PEC pedestal. ....	62
14. Example of a tapered impedance sheet based on a Kapton KC film substrate. ....	64
15. Theoretical stepped flange waveguide setup where the gray substance represents the tapered R-card. ....	65
16. Experimental setup of the stepped waveguide and flanges. ....	67
17. Experimental setup variant of the 0.1 inch plates and sheets. ....	68
18. Experimental scattering parameters for the 0.1 inch aperture flange (top-left: empty plate, top-right: filled plate, bottom-left: sheet, bottom-right: X-band). ....	68
19. Real and imaginary components of the effective impedance for the 400 ohm R-card with a 0.1 inch aperture flange. ....	69
20. Real and imaginary components of the effective impedance for the 900 ohm R-card with a 0.1 inch aperture flange. ....	69
21. Real and imaginary components of the effective impedance for the 2000 ohm R-card with a 0.1 inch aperture flange. ....	70
22. Experimental setup variant of the 0.2 inch plates and sheets. ....	71
23. Experimental scattering parameters for the 0.2 inch aperture flange (top-left: empty plate, top-right: filled plate, bottom-left: sheet, bottom-right: X-band). ....	71
24. Real and imaginary components of the effective impedance for the 400 ohm R-card with a 0.2 inch aperture flange. ....	72

Figure	Page
25. Real and imaginary components of the effective impedance for the 900 ohm R-card with a 0.2 inch aperture flange. ....	73
26. Real and imaginary components of the effective impedance for the 2000 ohm R-card with a 0.2 inch aperture flange. ....	73
27. Experimental setup variant of the 0.3 inch plates and sheets. ....	74
28. Experimental scattering parameters for the 0.3 inch aperture flange (top-left: empty plate, top-right: filled plate, bottom-left: sheet, bottom-right: X-band). ....	75
29. Real and imaginary components of the effective impedance for the 400 ohm R-card with a 0.3 inch aperture flange. ....	76
30. Real and imaginary components of the effective impedance for the 900 ohm R-card with a 0.3 inch aperture flange. ....	76
31. Real and imaginary components of the effective impedance for the 2000 ohm R-card with a 0.3 inch aperture flange. ....	76
32. Percentage of first 10 modes to pass through the 0.3 inch stepped flange (top-left: empty plate flange, top-right: filled plate flange, bottom: sheet flange. ....	79

## List of Tables

Table	Page
1. Summary of Maximum Complex Impedance Error from the 0.1 inch Sheet Flange .....	70
2. Summary of Maximum Complex Impedance Error from the 0.2 inch Empty Plate Flange .....	73
3. Summary of Maximum Complex Impedance Error from the 0.2 inch Filled Plate Flange .....	74
4. Summary of Maximum Complex Impedance Error from the 0.2 inch Sheet Flange .....	74
5. Summary of Maximum Complex Impedance Error from the 0.3 inch Empty Plate Flange .....	77
6. Summary of Maximum Complex Impedance Error from the 0.3 inch Filled Plate Flange .....	77
7. Summary of Maximum Complex Impedance Error from the 0.3 inch Sheet Flange .....	77

ARTIFICIAL INHOMOGENEOUS TAPERED IMPEDANCE SHEET  
CHARACTERIZATION AND APPLICATIONS

## I. Introduction

In the past decade electromagnetic compatibility (EMC) issues have increased in stature as low emission and high immunity to interference have emerged as essential criteria for characterizing overall integrated circuit (IC) performance. Achieving low emissions and increased interference immunity, however, can be problematic as technological trends have a propensity to act in an opposing manner. For instance, advances in process integration, higher switching speeds, and more complex circuits generally result in ICs generating an increased amount of parasitic emissions. Similarly, immunity to electromagnetic interference (EMI) tends to decrease with reduced supply voltages and increasing numbers of interfaces. As a consequence, the EMC/EMI field at the component level has gained much attention to abet with IC design in order to achieve these two criterion[1].

### 1.1 Problem Statement

Resistive and impedance sheets find numerous uses in EMC and EMI applications. With recent advances in the production of carbon loaded dielectric films, such as the ability to simultaneously alter the real and imaginary components of an impedance sheet[2], novel impedance distributions can be realized. These new impedance distributions can allow for precision scattering and shielding control and manipulation, as will be demonstrated in this research. Additionally, recent interest in the scattering measurements of uniform impedance sheets wrapped about a polystyrene foam

cylinder was reported in [3]. For the purposes of the current analysis, the problem is intensified by the impedance sheet distribution having a general  $\phi$  dependency. While there exists an abundance of literature investigating resistive and impedance sheet surfaces and scattering [4]-[13], this study introduces an analytic approach for calculating the scattering characteristics from cylindrical sheet impedances having a  $\phi$  dependency.

Furthermore, the  $\phi$  dependency presents an additional degree of complexity for electromagnetic material characterization purposes. The process of determining the complex permittivity and permeability of a material typically requires the sample to be linear, homogeneous, and isotropic. The introduction of the  $\phi$  dependency explicitly violates the homogeneous requirement. To mitigate inhomogeneous effects a reduced aperture waveguide system will be presented. This stepped waveguide technique utilizes a modal analysis to account for the excited higher-order modes, effectively allowing smaller cross-sections of the  $\phi$ -varying impedance sheet to be characterized[14; 15].

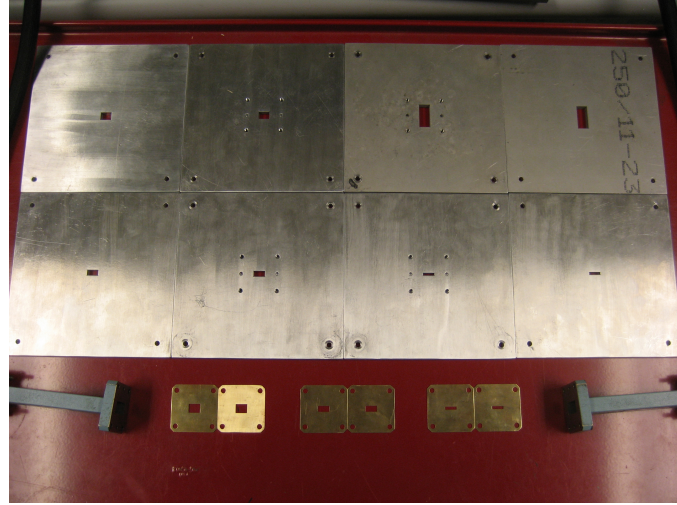


**Figure 1. Experimental setup variations of the full X-band plates, stepped aperture plates of 0.1, 0.2, 0.3 inches, and stepped aperture sheets of 0.1, 0.2, 0.3 inches.**

## 1.2 Limitations

Despite employing an analytical approach to determining the scattering and material characteristics from the  $\phi$ -varying impedance sheet, several practical aspects must be understood. For instance, the novel impedance sheet distributions necessary to attain precision scattering and shielding control and manipulation require ideal material values. Introducing realistic values diminishes the distribution effectiveness, such as frequency dependence. Additionally, the reduced aperture waveguide material characterization technique limits the amount of energy transmitted into the impedance sheet sample, thereby increasing the material characterization uncertainty. To exacerbate the problem an impedance sheet distribution containing high-loss aspects, to include low frequency measurements, can lead to total reflection with transmission measurements near the noise floor.

## 1.3 Scope

This research will include a theoretical development of the  $\text{TM}^z$  and  $\text{TE}^z$  field sets for a cylinder comprised of a  $\phi$ -dependent impedance sheet. General impedance sheet boundary conditions will be applied in addition to a Fourier series representation of the impedance sheet distribution. The utilization of Wronskian and recurrence relations will help to produce a computationally efficient matrix solution for the scattered field expansion coefficient  $a_n$ . This scattering coefficient  $a_n$  will then be included in the development of a two-dimensional scattering width, resulting in the scattering patterns of arbitrary diameter cylinder impedance sheet distributions. Then, the ability to adapt sheet impedances to effectively control the overall nulls in the bistatic scattering pattern will be demonstrated. Lastly, the electromagnetic material characterization aspect will focus on X-band frequencies (8.2 to 12.4 GHz) within a rectangular waveguide system, where a Newton-Raphson root search algorithm

will iteratively compute the complex permittivity of the non-magnetic  $\phi$ -dependent impedance sheet.

## 1.4 Thesis Organization

Chapter 2 provides the necessary theoretical background beginning with constitutive parameters and relations and Maxwell's equations in time-harmonic form, deriving the impedance boundary condition, and leading to the computationally-efficient incident  $TM^z$  and  $TE^z$  field sets. Chapter 3 derives an analytic approach for calculating the scattering characteristics from cylindrical sheet impedances having a  $\phi$  dependency with free-space filled, partially-filled perfect electric conductor (PEC), and general dielectric filled cases. Chapter 4 illustrates how impedance distributions can allow for precision scattering and shielding control and manipulation with experimentally measured complex material parameters. Finally, Chapter 5 provides a brief set of conclusions and recommendations for future research.

## II. Background Electromagnetic Theory

The study of electromagnetic field theory is concerned with charges in a general state of motion that produce electric and magnetic fields. The mathematical model that characterizes the relationship between the electromagnetic fields and the sources which maintain these fields is known as Maxwell's equations. For this research, all electromagnetic phenomena will be viewed from the macroscopic perspective, where the space-time average of sources and fields over regions and periods are large in comparison to atomic dimensions. Additionally, the rationalized mks system of units is employed. Finally, all theoretical development revealed in this chapter can be readily followed via [16]-[21].

### 2.1 Constitutive Parameters and Relations

Materials contain charged particles, such as electrons and protons, that necessarily interact with externally applied electric and magnetic fields based on their respective atomic structures. This interaction is physically characterized through constitutive parameters which define and mathematically model the relationship between charges and fields. These constitutive parameters are known as permittivity, permeability, and conductivity. The extent of this research assumes the complex cylindrical impedance sheet is immersed in simple medium (linear, homogeneous, and isotropic), as commonly defined as

$$\vec{M}_c = 0, \quad (1)$$

$$\vec{J}_c = \sigma \vec{E}, \quad (2)$$

$$\vec{D} = \epsilon \vec{E}, \quad (3)$$

$$\vec{B} = \mu \vec{H}, \quad (4)$$

where  $\vec{M}_c$  is the magnetic conduction current density (volts / square meter),  $\vec{J}_c$  is the electric conduction current density (Amperes / square meter),  $\sigma$  is the electric conductivity,  $\vec{D}$  is the electric flux density (Coulombs / square meter),  $\vec{E}$  is the electric field intensity (Volts / meter),  $\epsilon$  is the complex permittivity (Farads / meter),  $\vec{B}$  is the magnetic flux density (Webers / square meter),  $\vec{H}$  is the magnetic field intensity (Amperes / meter), and  $\mu$  is the complex permeability (Henries / meter).

For simple medium, the permittivity parameter  $\epsilon$  defines the susceptibility of a material to being polarized by an external electric field. Likewise, the permeability parameter  $\mu$  defines the susceptibility of a material to being magnetized by an external magnetic field. The conductivity parameter establishes the susceptibility of a material to sustain an electric ( $\sigma$ ) or fictitious magnetic ( $\sigma_m$ ) conduction current given an applied electric or magnetic field. Linearity relates the induced sources to the field strength; homogeneity describes the spatial variation; and isotropic means the induced currents are aligned with the applied fields.

## 2.2 Time-Harmonic Electromagnetic Fields

The theory and analysis presented in this research focuses solely on electromagnetic phenomena that vary sinusoidally in time. This steady-state sinusoidal time dependence leads to a mathematically simplified phasor notation of Maxwell's equations, such that

$$\nabla \times \vec{E}(\vec{r}, \omega) = -\vec{M}(\vec{r}, \omega) - j\omega \vec{B}(\vec{r}, \omega), \quad (5)$$

$$\nabla \times \vec{H}(\vec{r}, \omega) = \vec{J}(\vec{r}, \omega) + j\omega \vec{D}(\vec{r}, \omega), \quad (6)$$

$$\nabla \cdot \vec{D}(\vec{r}, \omega) = q_{ev}(\vec{r}, \omega), \quad (7)$$

$$\nabla \cdot \vec{B}(\vec{r}, \omega) = q_{mv}(\vec{r}, \omega), \quad (8)$$

where  $q_{ev}$  is the electric charge density,  $q_{mv}$  is the magnetic charge density,  $\vec{r}$  is the position vector, and  $\omega$  is the angular excitation frequency. Substituting (1)-(4) into (5)-(8) leads to the following (if source free)

$$\nabla \times \vec{E}(\vec{r}, \omega) = -j\omega\mu\vec{H}(\vec{r}, \omega), \quad (9)$$

$$\nabla \times \vec{H}(\vec{r}, \omega) = \sigma\vec{E} + j\omega\epsilon\vec{E}(\vec{r}, \omega), \quad (10)$$

$$\nabla \cdot \vec{E}(\vec{r}, \omega) = \frac{q_{ev}(\vec{r}, \omega)}{\epsilon}, \quad (11)$$

$$\nabla \cdot \vec{H}(\vec{r}, \omega) = \frac{q_{mv}(\vec{r}, \omega)}{\mu}, \quad (12)$$

which represents the time-harmonic Maxwell's equations in simple media.

### 2.2.1 Boundary Conditions.

The macroscopic electromagnetic field behavior across a boundary can be discontinuous. The boundary conditions for a generalized impedance sheet will be derived from Maxwell's equations. Boundary value problems explored in later sections will be solved via imposing the resulting conditions. A more complete understanding of the boundary conditions can illuminate the limitations and overall usefulness of the implemented technique.

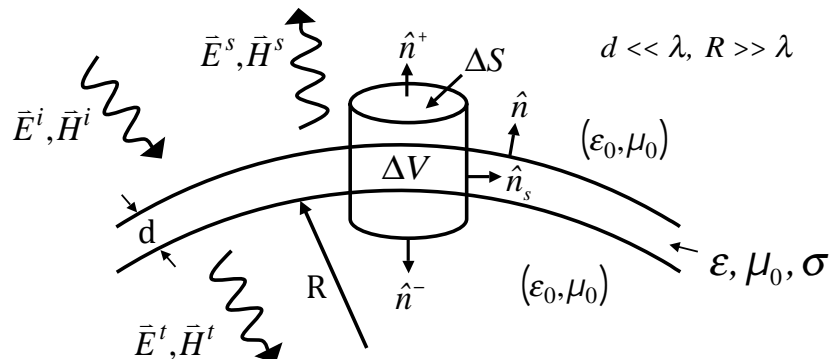


Figure 2. Impedance sheet boundary condition setup.

where  $\vec{E}^i, \vec{H}^i$  are the incident electric and magnetic fields,  $\vec{E}^s, \vec{H}^s$  are the scattered

electric and magnetic fields,  $\vec{E}^t, \vec{H}^t$  are the transmitted electric and magnetic fields,  $\epsilon_0$  is the free space permittivity,  $\mu_0$  is the free space permeability, and  $\lambda$  is the electromagnetic field's wavelength. Adapting (9) and (10) to the boundary, as shown in Figure 2, leads to the following formulation (assuming the impedance sheet is non-magnetic)

$$\nabla \times \vec{E} = -j\omega\mu_0 \vec{H}, \quad (13)$$

$$\nabla \times \vec{H} = \sigma \vec{E} + j\omega\epsilon \vec{E}. \quad (14)$$

Next, integrating (13) throughout the enclosed volume shown in Figure 2 and allowing the volume to approach zero produces

$$\lim_{\Delta V \rightarrow 0} \int_{\Delta V} \nabla \times \vec{E} dV = -j\omega\mu_0 \lim_{\Delta V \rightarrow 0} \int_{\Delta V} \vec{H} dV. \quad (15)$$

If  $\vec{H}$  is bounded as  $\Delta V \rightarrow 0$ , then the right-hand side of (15) goes to zero, mathematically shown as

$$-j\omega\mu_0 \lim_{\Delta V \rightarrow 0} \int_{\Delta V} \vec{H} dV = -j\omega\mu_0 \vec{H} \Delta V = 0. \quad (16)$$

Then, the Curl Theorem may be used to convert the volume integral of the remaining portion from (15) to a surface integral, such that

$$\oint_{\Delta S} \hat{n} \times \vec{E} dS = 0. \quad (17)$$

If the radius  $R$  is much larger than the electromagnetic wavelength, then the expres-

sion can be approximated such that

$$\oint_{\Delta S} \hat{n} \times \vec{E} dS \approx (\hat{n} \times \vec{E}^+ - \hat{n} \times \vec{E}^- + \hat{n}_s \times \vec{E}) \Delta S = 0, \quad (18)$$

where  $\vec{E}^\pm = \vec{E}(R^\pm, \phi)$  and  $\hat{n}$  is the unit outward normal. Here, large contrast is the key, depicted as

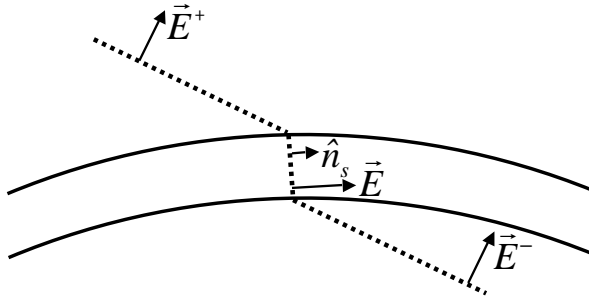


**Figure 3. High contrast electric field at the impedance boundary.**

where  $\vec{E}$  is the tangential electric field. The large contrast results in  $\hat{n}_s \times \vec{E} = 0$  and leads to the following boundary condition

$$\hat{n} \times \vec{E}^+ = \hat{n} \times \vec{E}^-. \quad (19)$$

The second boundary condition may be found by first adding a zero sum pair of terms to the right-hand side of (14) resulting in

$$\nabla \times \vec{H} = \sigma \vec{E} + j\omega \epsilon \vec{E}, \quad (20)$$

$$= \sigma \vec{E} + j\omega \epsilon \vec{E} - j\omega \epsilon_0 \vec{E} + j\omega \epsilon_0 \vec{E}, \quad (21)$$

$$= \sigma_e \vec{E} + j\omega \epsilon_0 \vec{E}, \quad (22)$$

where  $\sigma_e = \sigma + j\omega(\epsilon - \epsilon_0)$ . This leads to the notion of effective or equivalent conductivity immersed in free-space. Then, in an analogous process, integrating (22) as the

volume approaches zero results in

$$\lim_{\Delta V \rightarrow 0} \int_{\Delta V} \nabla \times \vec{H} dV = \int_{\Delta V} \vec{J}_e dV + j\omega\epsilon_0 \int_{\Delta V} \vec{E} dV, \quad (23)$$

where the bounded equivalent conduction current is defined as  $\vec{J}_e = \sigma_e \vec{E}$ . With  $\vec{E}$  bounded the second right-hand term of (23) must go to zero as given by

$$j\omega\epsilon_0 \int_{\Delta V} \vec{E} dV = 0. \quad (24)$$

Again, the Curl Theorem may be applied to the effect that

$$\hat{n} \times (\vec{H}^+ - \vec{H}^-) \Delta S = \vec{J}_e \Delta V, \quad (25)$$

where the volume differential may be expanded in terms of a surface differential,  $\vec{J}_e \Delta V = \vec{J}_e d \Delta S = \vec{J}_{es} \Delta S$ . This results in (25) reducing such that

$$\hat{n} \times (\vec{H}^+ - \vec{H}^-) = \vec{J}_{es}. \quad (26)$$

If it is then assumed that the resistive-air interfacial contrast is sufficient, then an equivalent impedance can be introduced as

$$\vec{J}_{es} = \vec{J}_e d \quad (27)$$

$$= (\sigma_e \vec{E}_{tang}) d \quad (28)$$

$$= \frac{1}{Z_e} \vec{E}_{tang}, \quad (29)$$

where  $\vec{E}_{tang}$  is the tangential electric field and the equivalent impedance is defined as  $Z_e = \frac{1}{\sigma_e d}$ . Substituting (29) into (26) leads to the following boundary condition

formulation

$$\hat{n} \times (\hat{n} \times \vec{E}^\pm) = -Z_e \hat{n} \times (\vec{H}^+ - \vec{H}^-). \quad (30)$$

As a set of equations both (19) and (30) constitute generalized approximate boundary conditions for a thin non-magnetic impedance structure. To summarize, the generalized impedance boundary conditions are presented as

$$\hat{n} \times \vec{E}^+ = \hat{n} \times \vec{E}^- \quad (31)$$

$$\hat{n} \times (\hat{n} \times \vec{E}^\pm) = -Z_e \hat{n} \times (\vec{H}^+ - \vec{H}^-). \quad (32)$$

In the physical sense, (31) implies that the electric field is continuous across the impedance sheet, while (32) indicates that the magnetic field is discontinuous across the impedance boundary by the amount of electric current induced in the impedance sheet. This can be readily perceived with an equivalent circuit theory model.

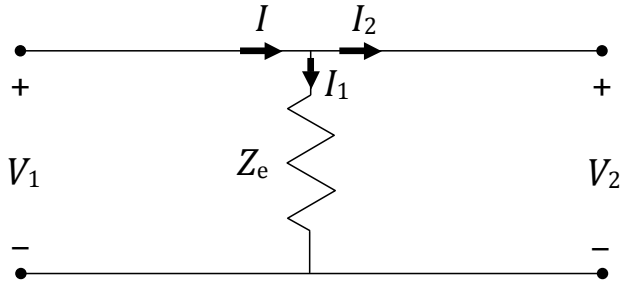


**Figure 4. Impedance sheet boundary condition circuit analogy.**

Figure 4 models the electrically thin impedance sheet with a lumped impedance element ( $Z_e$ ) in a parallel configuration. The electric fields on either side of the boundary are represented by the voltages  $V_1$  and  $V_2$  and are equal in the parallel configuration. The magnetic fields, represented by the currents, illustrate how the

current from  $V_1$  to  $V_2$  is discontinuous by the amount of shunt current that flows through the parallel impedance element  $Z_e$ .

## 2.3 Scattering by Cylinders

The extent of this research will focus on modal analysis for field solutions. In particular the scattering characteristics from cylindrical sheet impedances having a  $\phi$  dependency will be explored. The development utilizes a two-dimensional approach in order to obtain a meaningful solution with an accompanied physical intuition not readily apparent or attainable from a three-dimensional development. For practical implementation an approximate 2D-to-3D expansion may be employed

$$\sigma_{3D} \approx \sigma_{2D} \frac{2L^2}{\lambda}, \quad (33)$$

where  $L$  is the physical height of the cylinder, which is assumed to be suitably located for broadside illumination.

### 2.3.1 Electromagnetic Scattering Methodologies.

Electromagnetic scattering concerns the phenomena of an impressed source excitation inducing charges and currents on a structure, which then re-emits the energy in the form of electromagnetic waves. The general approach to a solution is to determine the scattered fields  $\vec{E}^s$ ,  $\vec{H}^s$  since they can then be utilized for RCS, radiation pattern, and impedance calculations. With many existing methods for determining the scattered fields, the particular choice method typically depends upon the geometrical shape and electrical size of the scattering body. These techniques are classified analytic, low-frequency, or high-frequency methods. For this research, an analytic method based upon a series expansion will be implemented. Essentially, the modal expansion technique is a field-based approach such that the fields are expanded in

infinite series of modes where each mode is a solution to the wave equation. Boundary condition enforcement results in infinite-series expansion coefficients which can then be applied to achieve an exact infinite-series solution for the scattered fields. This technique has inherent advantages and disadvantages. It is exact and rigorous but may be both computationally intensive and slow to converge if the scattering structure is much larger than the electromagnetic excitation frequency.

### 2.3.2 Wave Decoupling due to z-invariance.

With a two-dimensional approach the concept of invariance may be introduced. This requires two additional assumptions placed upon the problem setup. First, it necessitates that an excited electromagnetic wave be normally incident upon the cylinder. For the development of this analysis, the plane wave will be expressed as

$$\vec{E}^i(\vec{\rho}) = \hat{z}E_z^i(x) = \hat{z}E_{0z}^i e^{-jk_0x}, \quad (34)$$

$$\vec{H}^i(\vec{\rho}) = \hat{z}H_z^i(x) = \hat{z}H_{0z}^i e^{-jk_0x}. \quad (35)$$

Second, the cylinder will be assumed to have a length infinite in extend in the  $\hat{z}$ -direction, as shown in Figure 5.

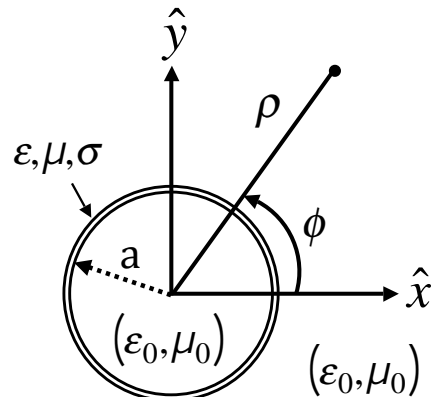


Figure 5. 2D z-invariance physical structure.

With both the geometrical structure and the excitation being  $z$ -invariant, the incident and scattered waves will decouple into two independent field sets,  $\text{TE}^z$  and  $\text{TM}^z$ . This is mathematically demonstrated by starting with Maxwell's equations and the continuity equations, such that

$$\nabla \times \vec{E} = -\vec{M} - j\omega\mu_0\vec{H}, \quad (36)$$

$$\nabla \times \vec{H} = \vec{J} + j\omega\epsilon_0\vec{E}, \quad (37)$$

$$\nabla \cdot \vec{D} = q_{ev}, \quad (38)$$

$$\nabla \cdot \vec{B} = q_{mv}, \quad (39)$$

Due to the inherent  $z$ -invariance of the problem, the  $\hat{z}$  component of the differential operator is eliminated,  $\frac{\delta}{\delta z} = 0$ . This is not to say that a  $\hat{z}$ -polarized electric field cannot exist, but rather that if it does then  $\vec{E}_z$  must be constant for all  $\hat{z}$ . This causes the differential operator (for cylindrical coordinates) to reduce such that

$$\nabla_t = \hat{\rho}\frac{\delta}{\delta\rho} + \hat{\phi}\frac{1}{\rho}\frac{\delta}{\delta\phi}, \quad (40)$$

where the  $t$  subscript has been adopted to indicate a transverse operator. Applying (40) to (36)-(39) and the continuity equations results in

$$\nabla_t \times (\vec{E}_t + \hat{z}E_z) = -(\vec{M}_t + \hat{z}M_z) - j\omega\mu_0(\vec{H}_t + \hat{z}H_z), \quad (41)$$

$$\nabla_t \times (\vec{H}_t + \hat{z}H_z) = (\vec{J}_t + \hat{z}J_z) + j\omega\epsilon_0(\vec{E}_t + \hat{z}E_z), \quad (42)$$

$$\nabla_t \cdot (\vec{E}_t + \hat{z}E_z) = \frac{q_{ev}}{\epsilon_0}, \quad \nabla_t \cdot (\vec{J}_t + \hat{z}J_z) = -j\omega q_{ev}, \quad (43)$$

$$\nabla_t \cdot (\vec{H}_t + \hat{z}H_z) = \frac{q_{mv}}{\mu_0}, \quad \nabla_t \cdot (\vec{M}_t + \hat{z}M_z) = -j\omega q_{mv}. \quad (44)$$

Expanding and grouping terms in each equation leads to

$$\nabla_t \times \vec{E}_t + \nabla_t \times \hat{z}E_z = -\vec{M}_t - j\omega\mu_0\vec{H}_t - \hat{z}M_z - \hat{z}j\omega\mu_0H_z, \quad (45)$$

$$\nabla_t \times \vec{H}_t + \nabla_t \times \hat{z}H_z = \vec{J}_t + j\omega\epsilon_0\vec{E}_t + \hat{z}J_z + \hat{z}j\omega\epsilon_0E_z, \quad (46)$$

$$\nabla_t \cdot \vec{E}_t = \frac{q_{ev}}{\epsilon_0}, \quad \nabla_t \cdot \vec{J}_t = -j\omega q_{ev}, \quad (47)$$

$$\nabla_t \cdot \vec{H}_t = \frac{q_{mv}}{\mu_0}, \quad \nabla_t \cdot \vec{M}_t = -j\omega q_{mv}. \quad (48)$$

Next equating transverse and longitudinal terms in the curl equations and identifying transverse component terms in the divergence and continuity equations leads to the following decoupled, independent sets of equations

$$\text{TE}^z = \begin{cases} \nabla_t \times \vec{E}_t = -\hat{z}M_z - \hat{z}j\omega\mu_0H_z \\ \nabla_t \times \hat{z}H_z = \vec{J}_t + j\omega\epsilon_0\vec{E}_t \\ \nabla_t \cdot \vec{E}_t = \frac{q_{ev}}{\epsilon_0} = \frac{-\nabla_t \cdot \vec{J}_t}{j\omega\epsilon_0} \end{cases}, \quad (49)$$

$$\text{TM}^z = \begin{cases} \nabla_t \times \vec{H}_t = \hat{z}J_z + \hat{z}j\omega\epsilon_0E_z \\ \nabla_t \times \hat{z}E_z = -\vec{M}_t - j\omega\mu_0\vec{H}_t \\ \nabla_t \cdot \vec{H}_t = \frac{q_{mv}}{\mu_0} = \frac{-\nabla_t \cdot \vec{M}_t}{j\omega\mu_0} \end{cases}, \quad (50)$$

where the Duality theorem principle holds and can be applied to interchange between the two field sets. The process of equating the terms above relied on the inherent linear independence of the field components.

## 2.4 Cylindrical Wave Transformations and Theorems

In order to simplify boundary condition enforcement for the cylindrical scatterers, various cylindrical wave transformations and theorems will be adopted. Using the

geometry presented in Figure 5, an incident plane wave can be represented as

$$\vec{E}^i(\vec{\rho}) = \hat{z}E_z^i(x) = \hat{z}E_{0z}^i e^{-jk_0\rho \cos \phi}, \quad (51)$$

$$\vec{H}^i(\vec{\rho}) = \hat{z}H_z^i(x) = \hat{z}H_{0z}^i e^{-jk_0\rho \cos \phi}, \quad (52)$$

if  $\vec{E}^i, \vec{H}^i$  is propagating along the  $+\hat{x}$  direction, for the  $\text{TM}^z$  and  $\text{TE}^z$  fields respectively. For the cylindrical wave transformation, representing the  $e^{-jk\rho \cos \phi}$  term as Bessel functions will take into account the radial dependence while periodic functions account for the  $\phi$ -variation. To maintain field generality the origin must be included, which disallows the use of Bessel functions of the second kind. Additionally, the periodicity requirement can be satisfied via a  $e^{jn\phi}$  term. This leads to the following mathematical representation

$$e^{-jk_0\rho \cos \phi} = \sum_{n=-\infty}^{\infty} a_n J_n(k_0\rho) e^{jn\phi}. \quad (53)$$

The unknown expansion coefficient  $a_n$  can then be found via integrating both sides of (53) by the operator  $\int_0^{2\pi} e^{-jm\phi} \{ \} d\phi$ , resulting in

$$\int_0^{2\pi} e^{-jk_0\rho \cos \phi} e^{-jm\phi} d\phi = \sum_{n=-\infty}^{\infty} a_n J_n(k_0\rho) \int_0^{2\pi} e^{j(n-m)\phi} d\phi, \quad (54)$$

where

$$\int_0^{2\pi} e^{j(n-m)\phi} d\phi = \begin{cases} 2\pi & \dots n = m \\ 0 & \dots n \neq m \end{cases}. \quad (55)$$

Ignoring the trivial case leads to the following formulation (for  $n = m$ )

$$\int_0^{2\pi} e^{-jk_0\rho \cos \phi} e^{-jm\phi} d\phi = a_m 2\pi J_m(k\rho). \quad (56)$$

Reindexing (56) and applying the following definition and identity

$$J_n(k_0\rho) = \frac{j^{-n}}{2\pi} \int_0^{2\pi} e^{-jk_0\rho \cos \phi} e^{jn\phi} d\phi, \quad (57)$$

$$J_n(k_0\rho) = J_{-n}(-k_0\rho) \quad (58)$$

leads to

$$2\pi j^{-n} J_n(k_0\rho) = a_n 2\pi J_n(k_0\rho). \quad (59)$$

Thus,  $a_n = j^{-n}$  and the cylindrical wave function representation of the plane wave can be written as

$$e^{-jk_0\rho \cos \phi} = \sum_{n=-\infty}^{\infty} j^{-n} J_n(k_0\rho) e^{jn\phi}. \quad (60)$$

It then follows that the incident electromagnetic fields for the  $TM^z$  and  $TE^z$  case can be written as

$$\vec{E}^i(\vec{\rho}) = \hat{z} E_{0z}^i e^{-jk_0 x} = \hat{z} E_{0z}^i \sum_{n=-\infty}^{\infty} j^{-n} J_n(k_0\rho) e^{jn\phi}, \quad (61)$$

$$\vec{H}^i(\vec{\rho}) = \hat{z} H_{0z}^i e^{-jk_0 x} = \hat{z} H_{0z}^i \sum_{n=-\infty}^{\infty} j^{-n} J_n(k_0\rho) e^{jn\phi}, \quad (62)$$

which can be manipulated into a more computationally efficient form through the use of certain Bessel function properties, as shown in Appendix A, represented as

$$\vec{E}^i(\vec{\rho}) = \hat{z} E_{0z}^i e^{-jk_0 x} = \hat{z} E_{0z}^i \sum_{n=0}^{\infty} \epsilon_n j^{-n} J_n(k_0\rho) \cos n\phi, \quad (63)$$

$$\vec{H}^i(\vec{\rho}) = \hat{z} H_{0z}^i e^{-jk_0 x} = \hat{z} H_{0z}^i \sum_{n=0}^{\infty} \epsilon_n j^{-n} J_n(k_0\rho) \cos n\phi, \quad (64)$$

where

$$\epsilon_n = \begin{cases} 1 & \dots n = 0 \\ 2 & \dots n \neq 0 \end{cases} . \quad (65)$$

#### 2.4.1 TM<sup>z</sup> Polarization Development.

For TM<sup>z</sup> polarization, the incident electric field expressed in (63) can be used to determine the incident magnetic field components. With the incident electric field in a convenient cylindrical wave-transformation form, the previously developed z-invariant Faraday's law may be applied to find the incident magnetic field. Additionally it can be assumed that the TM<sup>z</sup> incident field is maintained solely by a physically realizable impressed  $\hat{z}$ -directed current density  $J_z^i$  with  $\vec{M}_t^i = 0$ . Thus, the incident magnetic field can be found from (50) via

$$\vec{H}_t^i = \frac{-\nabla_t \times (\hat{z}E_z^i)}{j\omega\mu_0} \quad (66)$$

$$= \frac{\hat{z} \times \nabla_t E_z^i}{j\omega\mu_0} \quad (67)$$

$$= \frac{1}{jk_0\eta_0} \hat{z} \times (\hat{\rho} \frac{\delta E_z^i}{\delta \rho} + \hat{\phi} \frac{1}{\rho} \frac{\delta E_z^i}{\delta \phi}) \quad (68)$$

$$= \frac{1}{jk_0\eta_0} \hat{z} \times (\hat{\rho} k_0 \frac{\delta E_z^i}{\delta (k_0 \rho)} + \hat{\phi} \frac{1}{\rho} \frac{\delta E_z^i}{\delta \phi}) \quad (69)$$

$$= -\hat{\rho} \frac{1}{jk_0\eta_0 \rho} \frac{\delta E_z^i}{\delta \phi} + \hat{\phi} \frac{1}{j\eta_0} \frac{\delta E_z^i}{\delta (k_0 \rho)}. \quad (70)$$

The magnetic field components in computationally efficient form may then be

found by substituting (63) into (70), such that

$$H_\rho^i = -\frac{1}{jk_0\eta_0\rho} \frac{\delta E_z^i}{\delta\phi} \quad (71)$$

$$= -\frac{1}{jk_0\eta_0\rho} \frac{\delta}{\delta\phi} \left[ E_{0z}^i \sum_{n=0}^{\infty} \epsilon_n j^{-n} J_n(k_0\rho) \cos n\phi \right] \quad (72)$$

$$= \frac{2E_{0z}^i}{jk_0\eta_0\rho} \sum_{n=1}^{\infty} n j^{-n} J_n(k_0\rho) \sin n\phi, \quad (73)$$

$$H_\phi^i = \frac{1}{j\eta_0} \frac{\delta E_z^i}{\delta(k_0\rho)} \quad (74)$$

$$= \frac{1}{j\eta_0} \frac{\delta}{\delta(k_0\rho)} \left[ E_{0z}^i \sum_{n=0}^{\infty} \epsilon_n j^{-n} J_n(k_0\rho) \cos n\phi \right] \quad (75)$$

$$= \frac{E_{0z}^i}{j\eta_0} \sum_{n=0}^{\infty} \epsilon_n j^{-n} J'_n(k_0\rho) \cos n\phi. \quad (76)$$

To summarize, the  $\text{TM}^z$  incident electromagnetic field components expressed in computationally efficient form are shown below

$$E_z^i(\rho, \phi) = E_{0z}^i \sum_{n=0}^{\infty} \epsilon_n j^{-n} J_n(k_0\rho) \cos n\phi, \quad (77)$$

$$H_\rho^i(\rho, \phi) = \frac{2E_{0z}^i}{jk_0\eta_0\rho} \sum_{n=1}^{\infty} n j^{-n} J_n(k_0\rho) \sin n\phi, \quad (78)$$

$$H_\phi^i(\rho, \phi) = \frac{E_{0z}^i}{j\eta_0} \sum_{n=0}^{\infty} \epsilon_n j^{-n} J'_n(k_0\rho) \cos n\phi. \quad (79)$$

#### 2.4.2 $\text{TE}^z$ Polarization Development.

For  $\text{TE}^z$  polarization, the incident magnetic field expressed in (64) can be used to determine the incident electric field components. With the incident magnetic field in a convenient cylindrical wave-transformation form, the previously developed z-invariant Ampere's law may be applied to find the incident magnetic field. Additionally it can be assumed that the  $\text{TE}^z$  incident field is maintained solely by an impressed  $\hat{z}$ -directed current density  $M_z^i$  with  $\vec{J}_t^i = 0$ . Thus, the incident electric field can be found from

(49) via

$$\vec{E}_t^i = \frac{\nabla_t \times (\hat{z} H_z^i)}{j\omega\epsilon_0} \quad (80)$$

$$= \frac{\hat{z} \times \nabla_t H_z^i}{j\omega\epsilon_0} \quad (81)$$

$$= \frac{\eta_0}{jk_0} \hat{z} \times (\hat{\rho} \frac{1}{\rho} \frac{\delta H_z^i}{\delta \rho} + \hat{\phi} \frac{\delta H_z^i}{\delta \phi}) \quad (82)$$

$$= \frac{\eta_0}{jk_0} \hat{z} \times (\hat{\rho} \frac{k}{\rho} \frac{\delta H_z^i}{\delta (k_0 \rho)} + \hat{\phi} \frac{\delta H_z^i}{\delta \phi}) \quad (83)$$

$$= \hat{\rho} \frac{\eta_0}{jk_0 \rho} \frac{\delta H_z^i}{\delta \phi} - \hat{\phi} \frac{\eta_0}{j} \frac{\delta H_z^i}{\delta (k_0 \rho)}. \quad (84)$$

The magnetic field components in computationally efficient form may then be found by substituting (64) into (84), such that

$$E_\rho^i = \frac{\eta_0}{jk_0 \rho} \frac{\delta H_z^i}{\delta \phi} \quad (85)$$

$$= \frac{\eta_0}{jk_0 \rho} \frac{\delta}{\delta \phi} [H_{0z}^i \sum_{n=0}^{\infty} \epsilon_n j^{-n} J_n(k_0 \rho) \cos n\phi] \quad (86)$$

$$= \frac{-2H_{0z}^i \eta_0}{jk_0 \rho} \sum_{n=1}^{\infty} n j^{-n} J_n(k_0 \rho) \sin n\phi, \quad (87)$$

$$E_\phi^i = -\frac{\eta_0}{j} \frac{\delta H_z^i}{\delta (k_0 \rho)} \quad (88)$$

$$= -\frac{\eta_0}{j} \frac{\delta}{\delta (k_0 \rho)} [H_{0z}^i \sum_{n=0}^{\infty} \epsilon_n j^{-n} J_n(k_0 \rho) \cos n\phi] \quad (89)$$

$$= j H_{0z}^i \eta_0 \sum_{n=0}^{\infty} \epsilon_n j^{-n} J'_n(k_0 \rho) \cos n\phi. \quad (90)$$

To summarize, the  $TE^z$  incident electromagnetic field components expressed in com-

putationally efficient form are shown below

$$H_z^i(\rho, \phi) = E_{0z}^i \sum_{n=0}^{\infty} \epsilon_n j^{-n} J_n(k_0 \rho) \cos n\phi, \quad (91)$$

$$E_{\rho}^i(\rho, \phi) = \frac{-2H_{0z}^i \eta_0}{jk_0 \rho} \sum_{n=1}^{\infty} n j^{-n} J_n(k_0 \rho) \sin n\phi, \quad (92)$$

$$E_{\phi}^i(\rho, \phi) = j H_{0z}^i \eta_0 \sum_{n=0}^{\infty} \epsilon_n j^{-n} J'_n(k_0 \rho) \cos n\phi. \quad (93)$$

### III. Analytical Methodology

This research will demonstrate the ability to adapt sheet impedances to effectively control the overall nulls in the bistatic scattering pattern. Utilizing a cylinder comprised of a  $\phi$ -dependent impedance sheet provides for an additional degree of complexity beyond uniform impedance sheets. This additional complexity, however, prevents a closed-form solution from being easily obtained. The general approach to achieving a modal solution is to define the electromagnetic fields for all regions in a suitable representation, enforce appropriate boundary conditions, and solve for the scattered field expansion coefficient. With this scheme an orthogonal testing operator is typically utilized, after enforcing the boundary conditions, to identify only those electromagnetic modes, or field configurations, which satisfy both Maxwell's equations and the boundary conditions. This leads to a unique and physically meaningful solution. The complexity of the  $\phi$ -dependent impedance sheet, however, precludes the testing operator from sifting through the infinite number of modes. Hence, a computationally efficient approach will be utilized and demonstrated in the following section.

#### 3.1 Sheet Impedance Distribution Formulation

Expanding the impedance parameter  $Z_s(\phi)$  into a Fourier series will allow for a computationally-efficient formulation to identify the expansion coefficients. A suitable and physically realizable representation for the impedance distribution about the cylinder to achieve this outcome is

$$Z_s(\phi) = \sum_{q=0}^Q \alpha_q \cos(q\phi + \beta_q). \quad (94)$$

An appropriate testing operator to later assist in readily determining the expansion

coefficients after boundary condition enforcement is

$$\frac{1}{\pi} \int_{-\pi}^{\pi} \cos m\phi \{ \} d\phi. \quad (95)$$

Applying (95) to (94), in addition to a  $\cos n\phi$  term extracted in advance from the computationally efficient  $\text{TM}^z$  and  $\text{TE}^z$  field sets, results in

$$C_{mn} = \frac{1}{\pi} \int_{-\pi}^{\pi} Z_s(\phi) \cos m\phi \cos n\phi d\phi, \quad (96)$$

where the  $C_{mn}$  label has been adopted to signify the two-element expansion in matrix form. This term can be further expanded and simplified such that

$$C_{mn} = \frac{1}{\pi} \int_{-\pi}^{\pi} Z_s(\phi) \cos m\phi \cos n\phi d\phi \quad (97)$$

$$= \frac{1}{\pi} \int_{-\pi}^{\pi} \sum_{q=0}^Q \alpha_q \cos(q\phi + \beta_q) \cos m\phi \cos n\phi d\phi \quad (98)$$

$$= \frac{1}{\pi} \sum_{q=0}^Q \alpha_q \int_{-\pi}^{\pi} \cos(q\phi + \beta_q) \cos m\phi \cos n\phi d\phi. \quad (99)$$

Within (99) the  $q$ -indexed term can be re-written utilizing a simple cosine identity as

$$\cos(q\phi + \beta_q) = \cos q\phi \cos \beta_q - \sin q\phi \sin \beta_q, \quad (100)$$

which can be substituted back in and arranged such that

$$C_{mn} = \frac{1}{\pi} \sum_{q=0}^Q \alpha_q \int_{-\pi}^{\pi} [\cos q\phi \cos \beta_q \cos m\phi \cos n\phi - \sin q\phi \sin \beta_q \cos m\phi \cos n\phi] d\phi, \quad (101)$$

$$\begin{aligned}
C_{mn} = \frac{1}{\pi} \sum_{q=0}^Q \alpha_q \left[ \cos \beta_q \int_{-\pi}^{\pi} \cos q\phi \cos m\phi \cos n\phi d\phi \dots \right. \\
\left. - \sin \beta_q \int_{-\pi}^{\pi} \sin q\phi \cos m\phi \cos n\phi d\phi \right].
\end{aligned} \tag{102}$$

Attention to the integration limits reveals that the sin and cos pair within the second term of (102) reduce to zero, or

$$\int_{-\pi}^{\pi} \sin q\phi \cos m\phi \cos n\phi d\phi = 0, \tag{103}$$

which simplifies (102) such that

$$C_{mn} = \frac{1}{\pi} \sum_{q=0}^Q \alpha_q \cos \beta_q \int_{-\pi}^{\pi} \cos q\phi \cos m\phi \cos n\phi d\phi. \tag{104}$$

Then, applying a cosine identity to the m and n indexed terms produces

$$\cos m\phi \cos n\phi = \frac{1}{2} [\cos(m+n)\phi + \cos(m-n)\phi], \tag{105}$$

which can then be substituted back into (104) as

$$C_{mn} = \frac{1}{2\pi} \sum_{q=0}^Q \alpha_q \cos \beta_q \left[ \int_{-\pi}^{\pi} \cos q\phi \cos(m+n)\phi d\phi + \int_{-\pi}^{\pi} \cos q\phi \cos(m-n)\phi d\phi \right]. \tag{106}$$

Finally, the following integral identity can be applied for further reduction,

$$\int_{-\pi}^{\pi} \cos m\phi \cos n\phi d\phi = \pi \delta_{mn}, \tag{107}$$

where  $m, n \neq 0$  and  $\delta_{mn}$  is the Kronecker delta. This leads to the final computationally

efficient formulation

$$C_{mn} = \frac{1}{2} \sum_{q=0}^Q \alpha_q \cos \beta_q [\delta_{q,m+n} + \delta_{q,m-n}], \quad (108)$$

where

$$\delta_{q,m\pm n} = \begin{cases} 1 & \dots q = m \pm n \\ 0 & \dots q \neq m \pm n \end{cases}. \quad (109)$$

In expanded matrix notation, this can be practically implemented such that (for  $m = 0, \dots, M$  and  $n = 0, \dots, N$ )

$$C_{mn} = \begin{bmatrix} C_{00} & C_{01} & \dots & C_{0N} \\ C_{10} & C_{11} & \dots & C_{1N} \\ \vdots & \vdots & \ddots & \vdots \\ C_{M0} & C_{M1} & \dots & C_{MN} \end{bmatrix}. \quad (110)$$

This computationally-efficient formulation, relying on the impedance parameter expansion into a Fourier series, can now be utilized during boundary condition enforcement in later sections. Note, in the case where the impedance sheet is  $\phi$ -invariant, the orthogonal testing operator leads to a simple single-element expression, which can be computationally expressed as a vector. When a  $\phi$ -dependency is introduced to the impedance sheet, the orthogonal testing operator's ineffectualness results in a two-element expression, which can be computationally expressed as a matrix.

### 3.2 Free-space Filled Tapered Cylindrical Impedance Sheet

Consider an arbitrary plane wave normally incident along the  $\hat{x}$  direction on a cylinder infinite in extent in the  $\hat{z}$  direction, as illustrated in Figure 6. The cylinder, having radius  $a$ , is assumed to be electrically thin and is comprised of  $\phi$ -dependent high-contrast material parameters  $\epsilon, \mu_0, \sigma$ . Based on these assumptions, the cylinder can be modeled as a generalized  $\phi$ -dependent impedance sheet. Given that the dimensions of the physical scatterer are invariant along the  $\hat{z}$  direction as is the normally incident plane wave, the total fields decouple into two independent field sets,  $\text{TE}^z$  and  $\text{TM}^z$ . The following analysis will focus on the  $\text{TM}^z$  polarization set, followed by the  $\text{TE}^z$  case.

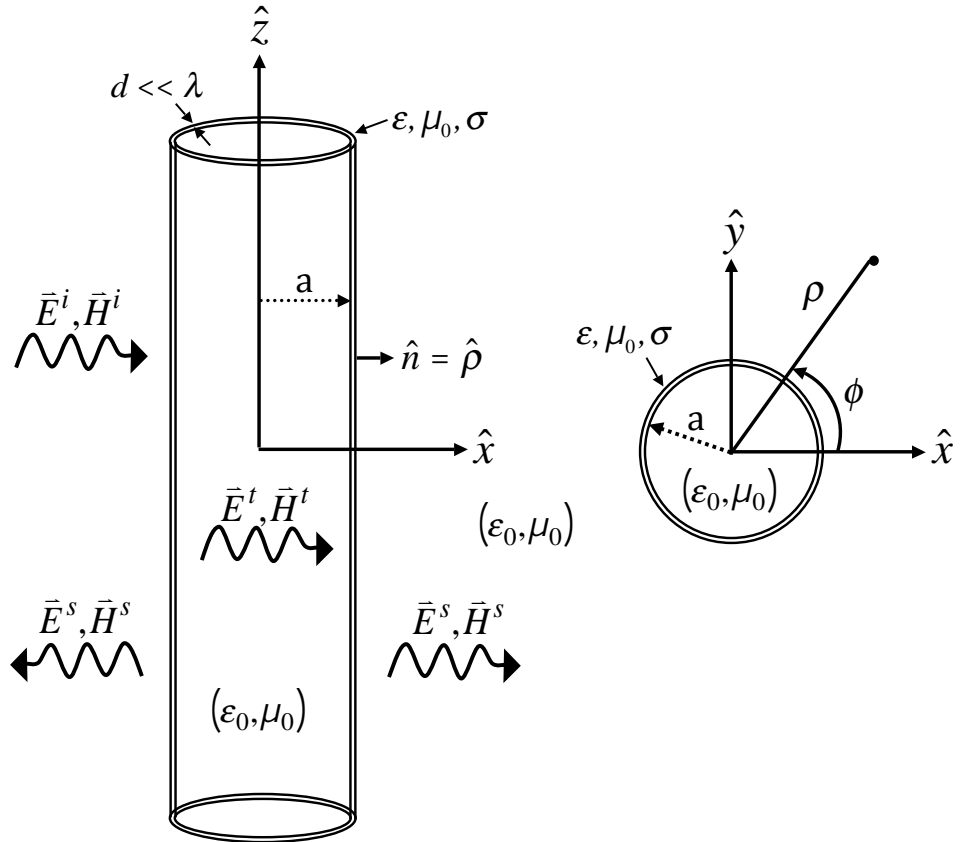


Figure 6. Side and top view of bistatic scattering from a cylinder comprised of a  $\phi$ -dependent impedance sheet.

### 3.2.1 $\text{TM}^z$ Polarization Development.

The  $\text{TM}^z$  incident electromagnetic field components expressed in computationally efficient form, as referenced from (77)-(79), are

$$E_z^i(\rho, \phi) = E_{0z}^i \sum_{n=0}^{\infty} \epsilon_n j^{-n} J_n(k_0 \rho) \cos n\phi, \quad (111)$$

$$H_\rho^i(\rho, \phi) = \frac{2E_{0z}^i}{jk_0 \eta_0 \rho} \sum_{n=1}^{\infty} n j^{-n} J_n(k_0 \rho) \sin n\phi, \quad (112)$$

$$H_\phi^i(\rho, \phi) = \frac{E_{0z}^i}{j\eta_0} \sum_{n=0}^{\infty} \epsilon_n j^{-n} J'_n(k_0 \rho) \cos n\phi, \quad (113)$$

$$\epsilon_n = \begin{cases} 1 & \text{if } n = 0 \\ 2 & \text{if } n \neq 0 \end{cases},$$

where  $k_0 = \omega \sqrt{\mu_0 \epsilon_0}$ ,  $\eta_0 = \sqrt{\mu_0 / \epsilon_0}$ ,  $\epsilon_n$  is the Neumann number,  $J_n$  is the Bessel function of the first kind of order  $n$  and  $H_n^{(2)}$  is the Hankel function of the second kind of order  $n$ .

The scattered field can be determined with knowledge of the incident field and the physical scatter. In this case, the z-invariant  $\text{TM}^z$  set formulation will induce a corresponding z-directed surface current density on the surface of the impedance sheet cylinder. This surface current density will maintain the scattered field and requires an appropriate mathematical representation. With a physical understanding of the scattering phenomena, it can be assumed that the scattered field will naturally radiate outward. This necessitates using Hankel functions of the second kind to represent the maintained outgoing waves. Additionally, utilizing the cosine function adequately and efficiently models the periodicity of the scattered field filling all angular space. Finally, the scattered field is ultimately maintained by the incident field and must therefore be proportional to the incident field strength. Thus, a suitable computationally efficient

representation to the scattered field is

$$E_z^s(\rho, \phi) = E_{0z}^i \sum_{n=0}^{\infty} a_n \epsilon_n j^{-n} H_n^{(2)}(k_0 \rho) \cos n\phi. \quad (114)$$

The magnetic field components in computationally efficient form may then be found by substituting (114) into (70), such that

$$H_\rho^s(\rho, \phi) = \frac{2E_{0z}^i}{jk_0 \eta_0 \rho} \sum_{n=1}^{\infty} a_n n j^{-n} H_n^{(2)}(k_0 \rho) \sin n\phi, \quad (115)$$

$$H_\phi^s(\rho, \phi) = \frac{E_{0z}^i}{j\eta_0} \sum_{n=0}^{\infty} a_n \epsilon_n j^{-n} H_n^{(2)'}(k_0 \rho) \cos n\phi. \quad (116)$$

The physical cylinder, being comprised of a  $\phi$ -varying impedance sheet, does not scatter the entirety of the incident field. The portion that is transmitted into the cylinder may be adduced from the previously discussed z-directed surface current density with the assumption that the impedance sheet is infinitesimally thin ( $d \ll \lambda$ ). This transmitted field will become a traveling standing wave within the cylinder and can be appropriately modeled with a Bessel function of the first kind. The same periodicity and proportionality requirements still hold, resulting in the following suitable computationally efficient transmitted field

$$E_z^t(\rho, \phi) = E_{0z}^i \sum_{n=0}^{\infty} b_n \epsilon_n j^{-n} J_n(k_0 \rho) \cos n\phi. \quad (117)$$

The magnetic field components in computationally efficient form may then be found by substituting (117) into (70), such that

$$H_\rho^t(\rho, \phi) = \frac{2E_{0z}^i}{jk_0 \eta_0 \rho} \sum_{n=1}^{\infty} b_n n j^{-n} J_n(k_0 \rho) \sin n\phi, \quad (118)$$

$$H_\phi^t(\rho, \phi) = \frac{E_{0z}^i}{j\eta_0} \sum_{n=0}^{\infty} b_n \epsilon_n j^{-n} J_n'(k_0 \rho) \cos n\phi. \quad (119)$$

With the electric and magnetic fields in all regions accounted for, the unknown expansion coefficients  $a_n$  and  $b_n$  can be found by invoking the impedance sheet boundary conditions, as referenced from (31) and (32),

$$\hat{n} \times \vec{E}^+ = \hat{n} \times \vec{E}^-, \quad (120)$$

$$\hat{n} \times (\hat{n} \times \vec{E}^\pm) = -Z_s(\phi) \hat{n} \times (\vec{H}^+ - \vec{H}^-), \quad (121)$$

where  $\vec{E}^\pm = \vec{E}(a^\pm, \phi)$ ,  $\vec{H}^\pm = \vec{H}(a^\pm, \phi)$ ,  $\hat{n}$  is the unit outward normal, and  $Z_s$  is the sheet impedance which is assumed to vary with  $\phi$  in this research. Substituting (111), (114), and (117) into (120) with  $\hat{n} = \hat{\rho}$  results in

$$\begin{aligned} E_{0z}^i \sum_{n=0}^{\infty} \epsilon_n j^{-n} J_n(k_0 a) \cos n\phi + E_{0z}^i \sum_{n=0}^{\infty} a_n \epsilon_n j^{-n} H_n^{(2)}(k_0 a) \cos n\phi = \\ E_{0z}^i \sum_{n=0}^{\infty} b_n \epsilon_n j^{-n} J_n(k_0 a) \cos n\phi \end{aligned} \quad (122)$$

Then, applying the testing operator (95) results in the following (for  $m = 0, \dots, \infty$ )

$$\begin{aligned} \sum_{n=0}^{\infty} J_n(k_0 a) \frac{\epsilon_n j^{-n}}{\pi} \int_{-\pi}^{\pi} \cos m\phi \cos n\phi d\phi + \sum_{n=0}^{\infty} a_n H_n^{(2)}(k_0 a) \frac{\epsilon_n j^{-n}}{\pi} \int_{-\pi}^{\pi} \cos m\phi \cos n\phi d\phi = \\ \sum_{n=0}^{\infty} b_n J_n(k_0 a) \frac{\epsilon_n j^{-n}}{\pi} \int_{-\pi}^{\pi} \cos m\phi \cos n\phi d\phi, \end{aligned} \quad (123)$$

where for  $m = n \neq 0$

$$\int_{-\pi}^{\pi} \cos m\phi \cos n\phi d\phi = \pi \delta_{mn}. \quad (124)$$

Substituting (124) into (123) produces

$$\sum_{n=0}^{\infty} \epsilon_n j^{-n} J_n(k_0 a) \delta_{mn} + \sum_{n=0}^{\infty} a_n \epsilon_n j^{-n} H_n^{(2)}(k_0 a) \delta_{mn} = \sum_{n=0}^{\infty} b_n \epsilon_n j^{-n} J_n(k_0 a) \delta_{mn}. \quad (125)$$

The Kronecker delta function effectively sifts through the infinite series summation to identify only those electromagnetic modes which satisfy both both Maxwell's equations and the boundary conditions, leading to the following relation

$$J_n(k_0 a) + a_n H_n^{(2)}(k_0 a) = b_n J_n(k_0 a). \quad (126)$$

Enforcing the second boundary condition will lead to an additional relation. Then, with two equations and two unknown expansion coefficients  $a_n$  and  $b_n$ , the scattered field can be determined. Hence, substituting (111), (113), (114), (116), and (119) into (121) with  $\hat{n} = \hat{\rho}$  results in

$$\begin{aligned} \hat{\rho} \times \left[ \hat{\rho} \times \hat{\phi} (E_z^i(a, \phi) + E_z^s(a, \phi)) \right] &= -Z_s(\phi) \hat{\rho} \times \hat{\phi} [H_\phi^i(a, \phi) + H_\phi^s(a, \phi) - H_\phi^t(a, \phi)], \\ -\hat{\rho} \times \hat{\phi} (E_z^i(a, \phi) + E_z^s(a, \phi)) &= -Z_s(\phi) \hat{\rho} \times \hat{\phi} [H_\phi^i(a, \phi) + H_\phi^s(a, \phi) - H_\phi^t(a, \phi)], \\ E_z^i(a, \phi) + E_z^s(a, \phi) &= Z_s(\phi) [H_\phi^i(a, \phi) + H_\phi^s(a, \phi) - H_\phi^t(a, \phi)], \end{aligned} \quad (127)$$

which can be further expanded as

$$\begin{aligned} E_{0z}^i \sum_{n=0}^{\infty} \epsilon_n j^{-n} \left[ J_n(k_0 a) + a_n H_n^{(2)}(k_0 a) \right] \cos n\phi &= \\ \frac{E_{0z}^i Z_s(\phi)}{j \eta_0} \sum_{n=0}^{\infty} \epsilon_n j^{-n} \left[ (1 - b_n) J'_n(k_0 a) + a_n H_n^{(2)'}(k_0 a) \right] \cos n\phi. \end{aligned} \quad (128)$$

The calculation of the field expansion coefficients  $a_n$  and  $b_n$  can be readily determined

by application of the previously utilized testing operator, resulting in

$$\sum_{n=0}^{\infty} \epsilon_n j^{-n} \left[ J_n(k_0 a) + a_n H_n^{(2)}(k_0 a) \right] \frac{1}{\pi} \int_{-\pi}^{\pi} \cos m\phi \cos n\phi d\phi = \\ \frac{1}{j\eta_0} \sum_{n=0}^{\infty} \epsilon_n j^{-n} \left[ (1 - b_n) J'_n(k_0 a) + a_n H_n^{(2)'}(k_0 a) \right] \frac{1}{\pi} \int_{-\pi}^{\pi} Z_s(\phi) \cos m\phi \cos n\phi d\phi. \quad (129)$$

This can then be further reduced by applying the Fourier series expansion of the impedance sheet, as developed in (94)-(110), such that

$$\sum_{n=0}^{\infty} \epsilon_n j^{-n} \left[ J_n(k_0 a) + a_n H_n^{(2)}(k_0 a) \right] \delta_{mn} = \\ \frac{1}{j\eta_0} \sum_{n=0}^{\infty} \epsilon_n j^{-n} \left[ (1 - b_n) J'_n(k_0 a) + a_n H_n^{(2)'}(k_0 a) \right] C_{mn}. \quad (130)$$

With two equations, (126) and (130), and two unknown expansion coefficients,  $a_n$  and  $b_n$ , the desired scattered field expansion coefficient can be readily found. Solving (126) for the expansion coefficient  $b_n$  leads to

$$b_n = 1 + a_n \frac{H_n^{(2)}(k_0 a)}{J_n(k_0 a)}, \quad (131)$$

which can then be substituted back into (130) producing

$$\sum_{n=0}^{\infty} j\eta_0 \epsilon_n j^{-n} \left[ J_n(k_0 a) + a_n H_n^{(2)}(k_0 a) \right] \delta_{mn} = \\ \sum_{n=0}^{\infty} \epsilon_n j^{-n} \left[ \left( 1 - 1 - a_n \frac{H_n^{(2)}(k_0 a)}{J_n(k_0 a)} \right) J'_n(k_0 a) + a_n H_n^{(2)'}(k_0 a) \right] C_{mn}, \quad (132)$$

$$\sum_{n=0}^{\infty} j\eta_0 \epsilon_n j^{-n} \left[ J_n(k_0 a) + a_n H_n^{(2)}(k_0 a) \right] \delta_{mn} = \\ \sum_{n=0}^{\infty} a_n \frac{\epsilon_n j^{-n}}{J_n(k_0 a)} \left[ J_n(k_0 a) H_n^{(2)'}(k_0 a) - J'_n(k_0 a) H_n^{(2)}(k_0 a) \right] C_{mn}. \quad (133)$$

This can be additionally simplified by utilizing Wronskian and recurrence relations,

as developed in Appendix B, where

$$J_n(k_0a)H_n^{(2)'}(k_0a) - J_n'(k_0a)H_n^{(2)}(k_0a) = -\frac{j^2}{\pi k_0a}. \quad (134)$$

This leads to a simplified expression for the scattered field expansion coefficient

$$\sum_{n=0}^{\infty} \eta_0 \epsilon_n j^{-n} J_n(k_0a) \delta_{mn} + \sum_{n=0}^{\infty} a_n \eta_0 \epsilon_n j^{-n} H_n^{(2)}(k_0a) \delta_{mn} = - \sum_{n=0}^{\infty} a_n \epsilon_n j^{-n} \frac{2C_{mn}}{\pi k_0 a J_n(k_0a)}. \quad (135)$$

Thus, a final formulation for the  $TM^z$  scattered field expansion coefficient can be found via

$$\sum_{n=0}^{\infty} a_n \epsilon_n j^{-n} \left[ H_n^{(2)}(k_0a) \delta_{mn} + \frac{2C_{mn}}{\pi \eta_0 k_0 a J_n(k_0a)} \right] = - \sum_{n=0}^{\infty} \epsilon_n j^{-n} J_n(k_0a) \delta_{mn}. \quad (136)$$

In expanded matrix notation, this can be practically implemented such that

$$\sum_{n=0}^N a_n D_{mn} = \sum_{m=0}^M E_m, \quad (137)$$

$$D_{mn} = \epsilon_n j^{-n} \left[ H_n^{(2)}(k_0a) \delta_{mn} + \frac{2C_{mn}}{\pi \eta_0 k_0 a J_n(k_0a)} \right], \quad (138)$$

$$E_m = -\epsilon_m j^{-m} J_m(k_0a). \quad (139)$$

$$\begin{bmatrix} D_{00} & D_{01} & \dots & D_{0N} \\ D_{10} & D_{11} & \dots & D_{1N} \\ \vdots & \vdots & \ddots & \vdots \\ D_{M0} & D_{M1} & \dots & D_{MN} \end{bmatrix} \begin{bmatrix} a_0 \\ a_1 \\ \vdots \\ a_M \end{bmatrix} = \begin{bmatrix} E_0 \\ E_1 \\ \vdots \\ E_M \end{bmatrix} \quad (140)$$

This result represents a matrix equation for the unknown scattered field expansion coefficients  $a_n$  in a readily solvable  $Ax = b$  form. Note, truncation becomes necessary to some value  $N$ , which is chosen in this work to be large enough to reach convergence

within a tolerance of  $1 \times 10^{-7}$ . With a suitable computationally efficient form achieved, the scattered field can be determined for any arbitrary impedance sheet distribution of a cylinder with a given  $\phi$  dependence.

This formulation can be verified by applying a special case. For instance, replacing the  $\phi$ -dependent impedance sheet with a PEC cylinder of identical dimensions ( $Z_s \rightarrow 0$ ), causes (136) to simplify to

$$\sum_{n=0}^{\infty} a_n \epsilon_n j^{-n} \left[ H_n^{(2)}(k_0 a) \delta_{mn} \right] = - \sum_{n=0}^{\infty} \epsilon_n j^{-n} J_n(k_0 a) \delta_{mn}, \quad (141)$$

where the scattered field expansion coefficient  $a_n$  can then be analytically solved for as

$$a_n = - \frac{J_n(k_0 a)}{H_n^{(2)}(k_0 a)}. \quad (142)$$

This expression is identically equal to the well-known  $TM^z$  scattered field expansion coefficient for a PEC and grants more confidence for the solution.

### 3.2.2 TE<sup>z</sup> Polarization Development.

The TE<sup>z</sup> incident electromagnetic field components expressed in computationally efficient form, as referenced from (91)-(93), are

$$H_z^i(\rho, \phi) = H_{0z}^i \sum_{n=0}^{\infty} \epsilon_n j^{-n} J_n(k_0 \rho) \cos n\phi, \quad (143)$$

$$E_{\rho}^i(\rho, \phi) = \frac{-2H_{0z}^i \eta_0}{jk_0 \rho} \sum_{n=1}^{\infty} n j^{-n} J_n(k_0 \rho) \sin n\phi, \quad (144)$$

$$E_{\phi}^i(\rho, \phi) = j H_{0z}^i \eta_0 \sum_{n=0}^{\infty} \epsilon_n j^{-n} J'_n(k_0 \rho) \cos n\phi. \quad (145)$$

$$\epsilon_n = \begin{cases} 1 & \text{if } n = 0 \\ 2 & \text{if } n \neq 0 \end{cases},$$

where  $k_0 = \omega \sqrt{\mu_0 \epsilon_0}$ ,  $\eta_0 = \sqrt{\mu_0 / \epsilon_0}$ ,  $\epsilon_n$  is the Neumann number,  $J_n$  is the Bessel function of the first kind of order  $n$  and  $H_n^{(2)}$  is the Hankel function of the second kind of order  $n$ .

The scattered field can be determined with knowledge of the incident field and the physical scatter. In this case, the z-invariant TE<sup>z</sup> set formulation will induce a corresponding z-directed surface current density on the surface of the impedance sheet cylinder. This surface current density, though fictitious, will represent how the scattered field is maintained and requires an appropriate mathematical representation. Thus, a suitable computationally efficient representation to the scattered field is

$$H_z^s(\rho, \phi) = H_{0z}^i \sum_{n=0}^{\infty} a_n \epsilon_n j^{-n} H_n^{(2)}(k_0 \rho) \cos n\phi. \quad (146)$$

The electric field components in computationally efficient form may then be

found by substituting (146) into (84), such that

$$E_\rho^s(\rho, \phi) = \frac{-2H_{0z}^i \eta_0}{jk_0 \rho} \sum_{n=1}^{\infty} a_n n j^{-n} H_n^{(2)}(k_0 \rho) \sin n\phi, \quad (147)$$

$$E_\phi^s(\rho, \phi) = j H_{0z}^i \eta_0 \sum_{n=0}^{\infty} a_n \epsilon_n j^{-n} H_n^{(2)'}(k_0 \rho) \cos n\phi. \quad (148)$$

Similarly, a suitable computationally efficient representation to the transmitted field is

$$H_z^t(\rho, \phi) = H_{0z}^i \sum_{n=0}^{\infty} b_n \epsilon_n j^{-n} J_n(k_0 \rho) \cos n\phi. \quad (149)$$

The electric field components in computationally efficient form may then be found by substituting (149) into (84), such that

$$E_\rho^t(\rho, \phi) = \frac{-2H_{0z}^i \eta_0}{jk_0 \rho} \sum_{n=1}^{\infty} b_n n j^{-n} J_n(k_0 \rho) \sin n\phi, \quad (150)$$

$$E_\phi^t(\rho, \phi) = j H_{0z}^i \eta_0 \sum_{n=0}^{\infty} b_n \epsilon_n j^{-n} J_n'(k_0 \rho) \cos n\phi. \quad (151)$$

With the electric and magnetic fields in all regions accounted for, the unknown expansion coefficients  $a_n$  and  $b_n$  can be found by invoking the impedance sheet boundary conditions, as referenced from (31) and (32),

$$\hat{n} \times \vec{E}^+ = \hat{n} \times \vec{E}^-, \quad (152)$$

$$\hat{n} \times (\hat{n} \times \vec{E}^\pm) = -Z_s(\phi) \hat{n} \times (\vec{H}^+ - \vec{H}^-), \quad (153)$$

where  $\vec{E}^\pm = \vec{E}(a^\pm, \phi)$ ,  $\vec{H}^\pm = \vec{H}(a^\pm, \phi)$ ,  $\hat{n}$  is the unit outward normal, and  $Z_s$  is the sheet impedance which is assumed to vary with  $\phi$  in this work. Substituting (144),

(145), (147), (148), (150), and (151) into (152) with  $\hat{n} = \hat{\rho}$  results in

$$jH_{0z}^i \eta \sum_{n=0}^{\infty} \epsilon_n j^{-n} J'_n(k_0 \rho) \cos n\phi + jH_{0z}^i \eta \sum_{n=0}^{\infty} a_n \epsilon_n j^{-n} H_n^{(2)'}(k_0 \rho) \cos n\phi = jH_{0z}^i \eta \sum_{n=0}^{\infty} b_n \epsilon_n j^{-n} J'_n(k_0 \rho) \cos n\phi. \quad (154)$$

The, applying the testing operator (95) results in the following (for  $m = 0, \dots, \infty$ )

$$\sum_{n=0}^{\infty} J'_n(k_0 \rho) \frac{\epsilon_n j^{-n}}{\pi} \int_{-\pi}^{\pi} \cos m\phi \cos n\phi d\phi + \sum_{n=0}^{\infty} a_n H_n^{(2)'}(k_0 \rho) \frac{\epsilon_n j^{-n}}{\pi} \int_{-\pi}^{\pi} \cos m\phi \cos n\phi d\phi = \sum_{n=0}^{\infty} b_n J'_n(k_0 \rho) \frac{\epsilon_n j^{-n}}{\pi} \int_{-\pi}^{\pi} \cos m\phi \cos n\phi d\phi, \quad (155)$$

where for  $m = n \neq 0$

$$\int_{-\pi}^{\pi} \cos m\phi \cos n\phi d\phi = \pi \delta_{mn}. \quad (156)$$

Substituting (156) into (155) produces the following relation

$$J'_n(k_0 a) + a_n H_n^{(2)'}(k_0 a) = b_n J'_n(k_0 a). \quad (157)$$

Applying the second boundary condition will lead to an additional relation. Then, with two equations and two unknown expansion coefficients  $a_n$  and  $b_n$ , the scattered field can be determined. Hence, substituting (143)-(145), (146)-(148), and (149)-(151)

into (153) with  $\hat{n} = \hat{\rho}$  results in

$$\hat{\rho} \times \left[ \hat{\rho} \times \left( \hat{\rho} E_\rho(a, \phi) + \hat{\phi} E_\phi(a, \phi) \right) \right] = -Z_s(\phi) \hat{\rho} \times \hat{z} [H_z^i(a, \phi) + H_z^s(a, \phi) - H_z^t(a, \phi)], \quad (158)$$

$$\hat{\rho} \times \hat{z} (E_\phi^i(a, \phi) + E_\phi^s(a, \phi)) = -Z_s(\phi) \hat{\rho} \times \hat{z} [H_z^i(a, \phi) + H_z^s(a, \phi) - H_z^t(a, \phi)], \quad (159)$$

$$E_\phi^i(a, \phi) + E_\phi^s(a, \phi) = -Z_s(\phi) [H_z^i(a, \phi) + H_z^s(a, \phi) - H_z^t(a, \phi)], \quad (160)$$

which can be further expanded as

$$\begin{aligned} jH_{0z}^i \eta \sum_{n=0}^{\infty} \epsilon_n j^{-n} \left[ J'_n(k_0 a) + a_n H_n^{(2)'}(k_0 a) \right] \cos(n\phi) = \\ -H_{0z}^i Z_s(\phi) \sum_{n=0}^{\infty} \epsilon_n j^{-n} \left[ (1 - b_n) J_n(k_0 a) + a_n H_n^{(2)}(k_0 a) \right] \cos(n\phi). \end{aligned} \quad (161)$$

Applying the testing operator (95) and the Fourier series expansion of the impedance sheet (96), results in

$$\begin{aligned} - \sum_{n=0}^{\infty} j\eta \epsilon_n j^{-n} \left[ J'_n(k_0 a) + a_n H_n^{(2)'}(k_0 a) \right] \delta_{mn} = \\ \sum_{n=0}^{\infty} \epsilon_n j^{-n} \left[ (1 - b_n) J_n(k_0 a) + a_n H_n^{(2)}(k_0 a) \right] C_{mn}. \end{aligned} \quad (162)$$

With two equations, (157) and (162), and two unknown expansion coefficients,  $a_n$  and  $b_n$ , the desired scattered field expansion coefficient can be readily found. Solving (157) for the expansion coefficient  $b_n$  leads to

$$b_n = 1 + a_n \frac{H_n^{(2)'}(k_0 a)}{J'_n(k_0 a)}, \quad (163)$$

which can then be substituted back into (162) producing

$$\begin{aligned}
& - \sum_{n=0}^{\infty} j\eta_0 \epsilon_n j^{-n} \left[ J'_n(k_0 a) + a_n H_n^{(2)'}(k_0 a) \right] \delta_{mn} = \\
& \quad \sum_{n=0}^{\infty} \epsilon_n j^{-n} \left[ \left( 1 - 1 - a_n \frac{H_n^{(2)'}(k_0 a)}{J'_n(k_0 a)} \right) J_n(k_0 a) + a_n H_n^{(2)}(k_0 a) \right] C_{mn}, \quad (164)
\end{aligned}$$

$$\begin{aligned}
& - \sum_{n=0}^{\infty} j\eta_0 \epsilon_n j^{-n} \left[ J'_n(k_0 a) + a_n H_n^{(2)'}(k_0 a) \right] \delta_{mn} = \\
& \quad \sum_{n=0}^{\infty} a_n \frac{\epsilon_n j^{-n}}{J'_n(k_0 a)} \left[ J'_n(k_0 a) H_n^{(2)}(k_0 a) - J_n(k_0 a) H_n^{(2)'}(k_0 a) \right] C_{mn}. \quad (165)
\end{aligned}$$

This can be additionally simplified by utilizing Wronskian and recurrence relations developed in Appendix B, where

$$J'_n(k_0 a) H_n^{(2)}(k_0 a) - J_n(k_0 a) H_n^{(2)'}(k_0 a) = \frac{j^2}{\pi k_0 a}. \quad (166)$$

This leads to a simplified expression for the scattered field expansion coefficient

$$\begin{aligned}
& - \sum_{n=0}^{\infty} \eta_0 \epsilon_n j^{-n} J'_n(k_0 a) \delta_{mn} - \sum_{n=0}^{\infty} a_n \eta_0 \epsilon_n j^{-n} H_n^{(2)'}(k_0 a) \delta_{mn} = \sum_{n=0}^{\infty} a_n \epsilon_n j^{-n} \frac{2C_{mn}}{\pi k_0 a J'_n(k_0 a)}. \\
& \quad (167)
\end{aligned}$$

Thus, a final formulation for the  $TE^z$  scattered field expansion coefficient can be found via

$$\sum_{n=0}^{\infty} a_n \epsilon_n j^{-n} \left[ H_n^{(2)'}(k_0 a) \delta_{mn} + \frac{2C_{mn}}{\pi \eta_0 k_0 a J'_n(k_0 a)} \right] = - \sum_{n=0}^{\infty} \epsilon_n j^{-n} J'_n(k_0 a) \delta_{mn}.$$

(168)

In expanded matrix notation, this can be practically implemented in (137) such that

$$D_{mn} = \epsilon_n j^{-n} \left[ H_n^{(2)'}(k_0 a) \delta_{mn} + \frac{2C_{mn}}{\pi \eta_0 k_0 a J_n'(k_0 a)} \right], \quad (169)$$

$$E_m = -\epsilon_m j^{-m} J_m'(k_0 a). \quad (170)$$

This formulation can be verified by applying a special case. For instance, replacing the  $\phi$ -dependent impedance sheet with a PEC cylinder of identical dimensions ( $Z_s \rightarrow 0$ ), causes (168) to simplify to

$$\sum_{n=0}^{\infty} a_n \epsilon_n j^{-n} \left[ H_n^{(2)'}(k_0 a) \delta_{mn} \right] = - \sum_{n=0}^{\infty} \epsilon_n j^{-n} J_n'(k_0 a) \delta_{mn}, \quad (171)$$

where the scattered field expansion coefficient  $a_n$  can then be analytically solved for as

$$a_n = - \frac{J_n'(k_0 a)}{H_n^{(2)'}(k_0 a)}. \quad (172)$$

This expression is identically equal to the well-known  $TE^z$  scattered field expansion coefficient for a PEC and grants more confidence for the solution.

### 3.3 PEC Filled Tapered Cylindrical Impedance Sheet

Consider a plane wave traveling along the forward  $x$  direction normally incident on a cylindrical structure that is infinite in extent along  $z$ , as illustrated in Fig. 7. The structure is comprised of an electrically-thin ( $d \ll \lambda$ ) cylindrical impedance sheet having radius  $a_1$  and an inner solid pedestal of radius  $a_2$ . The  $\phi$ -dependent high-contrast material parameters of the impedance sheet are  $\epsilon, \mu_0, \sigma$  and the pedestal is assumed to be comprised of a PEC. The regions  $a_2 < \rho < a_1$  and  $\rho > a_1$  are assumed to be free-space filled.

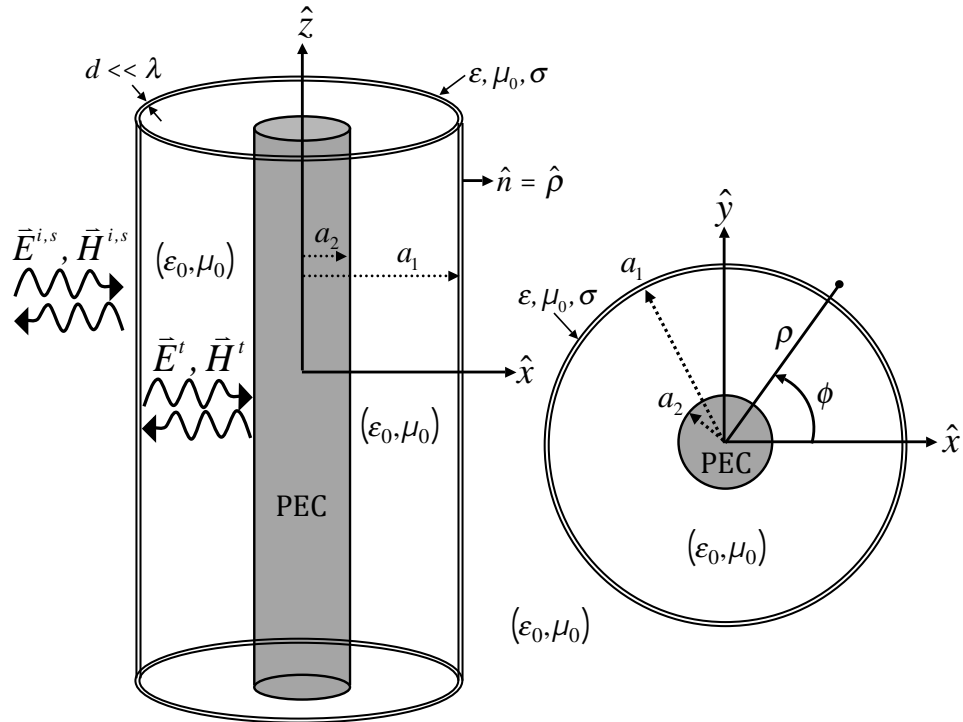


Figure 7. Side and top view of bistatic scattering from a cylinder comprised of a  $\phi$ -dependent impedance sheet wrapped about a PEC pedestal.

Since both the scattering structure and incident excitation are  $z$ -invariant, Maxwell's equations decouple into two independent field sets,  $\text{TE}^z$  and  $\text{TM}^z$ . In addition, based on the above assumptions, an impedance sheet boundary condition may be utilized to accommodate the scattering effects of the impedance sheet. The  $z$ -invariance and

impedance sheet boundary condition implementation greatly facilitates the analytical development for the bistatic scattering width calculations, as discussed next.

### 3.3.1 $\text{TM}^z$ Polarization Development.

For  $\text{TM}^z$  polarization, the tangential electric and magnetic field (i.e., incident plus scattered) components in the region  $\rho > a_1$  can be expressed according to (77)-(79) and (114)-(116) as (assuming an  $e^{j\omega t}$  time dependence)

$$E_z^{i,s}(\rho, \phi) = E_{0z}^i \sum_{n=0}^{\infty} \epsilon_n j^{-n} \left[ J_n(k_0 \rho) + a_n H_n^{(2)}(k_0 \rho) \right] \cos n\phi, \quad (173)$$

$$H_{\phi}^{i,s}(\rho, \phi) = \frac{E_{0z}^i}{j\eta_0} \sum_{n=0}^{\infty} \epsilon_n j^{-n} \left[ J'_n(k_0 \rho) + a_n H_n^{(2)'}(k_0 \rho) \right] \cos n\phi, \quad (174)$$

where  $k_0 = \omega \sqrt{\epsilon_0 \mu_0}$ ,  $\eta_0 = \sqrt{\mu_0 / \epsilon_0}$ ,  $\epsilon_n$  is the Neumann number,  $J_n$  is the Bessel function of the first kind of order  $n$ ,  $H_n^{(2)}$  is the Hankel function of the second kind of order  $n$  and the prime represents differentiation with respect to the argument. Similarly, the tangential fields in regions  $a_2 < \rho < a_1$  may be written as

$$E_z^t(\rho, \phi) = E_{0z}^i \sum_{n=0}^{\infty} \epsilon_n j^{-n} \left[ b_n J_n(k_0 \rho) + c_n H_n^{(2)}(k_0 \rho) \right] \cos n\phi, \quad (175)$$

$$H_{\phi}^t(\rho, \phi) = \frac{E_{0z}^i}{j\eta_0} \sum_{n=0}^{\infty} \epsilon_n j^{-n} \left[ b_n J'_n(k_0 \rho) + c_n H_n^{(2)'}(k_0 \rho) \right] \cos n\phi. \quad (176)$$

The unknown amplitude coefficients  $a_n$ ,  $b_n$ , and  $c_n$  are found via boundary condition enforcement at  $\rho = a_1$  and  $\rho = a_2$ . Note, the expansion coefficient of particular relevance for bistatic scattering width calculations is  $a_n$ . Enforcing continuity of the tangential electric and magnetic fields at the PEC interface (i.e.,  $\rho = a_2$ ) and applying the suitable testing operator results in

$$b_n J_n(k_0 a_2) + c_n H_n^{(2)}(k_0 a_2) = 0. \quad (177)$$

Next, it is necessary to enforce the impedance sheet boundary conditions

$$\hat{n} \times \vec{E}^+ = \hat{n} \times \vec{E}^-, \quad (178)$$

$$\hat{n} \times (\hat{n} \times \vec{E}^\pm) = -Z_s(\phi) \hat{n} \times (\vec{H}^+ - \vec{H}^-), \quad (179)$$

where  $\vec{E}^\pm = \vec{E}(a_1^\pm, \phi)$ ,  $\vec{H}^\pm = \vec{H}(a_1^\pm, \phi)$ ,  $\hat{n}$  is the unit outward normal, and  $Z_s$  is the sheet impedance which is assumed to vary with  $\phi$  in this work. Substituting (173)-(174) and (175)-(176) into (178) and (179) with  $\hat{n} = \hat{\rho}$  and applying the suitable testing operator leads to

$$J_n(k_0 a_1) + a_n H_n^{(2)}(k_0 a_1) = b_n J_n(k_0 a_1) + c_n H_n^{(2)}(k_0 a_1), \quad (180)$$

$$\begin{aligned} \sum_{n=0}^{\infty} j \eta_0 \epsilon_n j^{-n} \left[ J_n(k_0 a_1) + a_n H_n^{(2)}(k_0 a_1) \right] \delta_{mn} = \\ \sum_{n=0}^{\infty} \epsilon_n j^{-n} \left[ (1 - b_n) J'_n(k_0 a_1) + a_n H_n^{(2)'}(k_0 a_1) - c_n H_n^{(2)'}(k_0 a_1) \right] C_{mn} \end{aligned}, \quad (181)$$

where the substitution of the Fourier series expansion of the  $\phi$ -varying impedance sheet has been included. Solving (177) in terms of  $c_n$  results in

$$c_n = -b_n \frac{J_n(k_0 a_2)}{H_n^{(2)}(k_0 a_2)}, \quad (182)$$

which can then be substituted into (180) leading to the expression

$$b_n = \frac{J_n(k_0 a_1) + a_n H_n^{(2)}(k_0 a_1)}{J_n(k_0 a_1) - \frac{J_n(k_0 a_2)}{H_n^{(2)}(k_0 a_2)} H_n^{(2)}(k_0 a_1)}. \quad (183)$$

The desired  $TM^z$  scattered field expansion coefficients  $a_n$  are readily solved by substituting (182) and (183) into (181), leading with the inclusion of Wronskian and

recurrence relations to (for  $m = 0, \dots, N$ )

$$\boxed{- \sum_{n=0}^{\infty} \epsilon_n j^{-n} \left[ \pi k_0 \eta_0 a_1 J_n(k_0 a_1) \delta_{mn} + \frac{2 J_n(k_0 a_2) C_{mn}}{J_n(k_0 a_1) H_n^{(2)}(k_0 a_2) - J_n(k_0 a_2) H_n^{(2)}(k_0 a_1)} \right] = \sum_{n=0}^{\infty} a_n \epsilon_n j^{-n} \left[ \pi k_0 \eta_0 a_1 H_n^{(2)}(k_0 a_1) \delta_{mn} + \frac{2 H_n^{(2)}(k_0 a_2) C_{mn}}{J_n(k_0 a_1) H_n^{(2)}(k_0 a_2) - J_n(k_0 a_2) H_n^{(2)}(k_0 a_1)} \right].} \quad (184)$$

In expanded matrix notation, this can be practically implemented as in (137). This formulation can be verified analytically by employing a special case. If the PEC tube within the cylinder comprised of a  $\phi$ -dependent impedance sheet is removed, then (184) should identically reduce to (136). This can be readily accomplished by allowing the imposed PEC boundary condition, as referenced by (182), to equal zero, which leads to the following

$$\sum_{n=0}^{\infty} a_n \epsilon_n j^{-n} \left[ H_n^{(2)}(k_0 a_1) \delta_{mn} + \frac{2 C_{mn}}{\pi \eta_0 k_0 a_1 J_n(k_0 a_1)} \right] = - \sum_{n=0}^{\infty} \epsilon_n j^{-n} J_n(k_0 a_1) \delta_{mn}. \quad (185)$$

Thus, as the PEC tube within the cylinder comprised of a  $\phi$ -dependent impedance sheet is removed, then (184) reduces identically to (136) and grants more confidence for the solution.

### 3.3.2 TE<sup>z</sup> Polarization Development.

For TE<sup>z</sup> polarization, the tangential electric and magnetic field (i.e., incident plus scattered) components in the region  $\rho > a_1$  can be expressed according to (91)-(93) and (146)-(148) as (assuming an  $e^{j\omega t}$  time dependence)

$$H_z^{i,s}(\rho, \phi) = H_{0z}^i \sum_{n=0}^{\infty} \epsilon_n j^{-n} \left[ J_n(k_0 \rho) + a_n \epsilon_n j^{-n} H_n^{(2)}(k_0 \rho) \right] \cos n\phi, \quad (186)$$

$$E_{\phi}^{i,s}(\rho, \phi) = j H_{0z}^i \eta \sum_{n=0}^{\infty} \epsilon_n j^{-n} \left[ J'_n(k_0 \rho) + a_n \epsilon_n j^{-n} H_n^{(2)'}(k_0 \rho) \right] \cos n\phi. \quad (187)$$

where  $k_0 = \omega\sqrt{\epsilon_0\mu_0}$ ,  $\eta_0 = \sqrt{\mu_0/\epsilon_0}$ ,  $\epsilon_n$  is the Neumann number,  $J_n$  is the Bessel function of the first kind of order  $n$ ,  $H_n^{(2)}$  is the Hankel function of the second kind of order  $n$  and the prime represents differentiation with respect to the argument. Similarly, the tangential fields in regions  $a_2 < \rho < a_1$  may be written as

$$H_z^t(\rho, \phi) = H_{0z}^i \sum_{n=0}^{\infty} \epsilon_n j^{-n} \left[ b_n J_n(k_0 \rho) + c_n H_n^{(2)}(k_0 \rho) \right] \cos n\phi, \quad (188)$$

$$E_\phi^t(\rho, \phi) = j H_{0z}^i \eta_0 \sum_{n=0}^{\infty} \epsilon_n j^{-n} \left[ b_n J'_n(k_0 \rho) + c_n H_n^{(2)'}(k_0 \rho) \right] \cos n\phi. \quad (189)$$

The unknown amplitude coefficients  $a_n$ ,  $b_n$ , and  $c_n$  are found via boundary condition enforcement at  $\rho = a_1$  and  $\rho = a_2$ . Note, the expansion coefficient of particular relevance for bistatic scattering width calculations is  $a_n$ . Enforcing continuity of the tangential electric and magnetic fields at the PEC interface (i.e.,  $\rho = a_2$ ) and applying the suitable testing operator results in

$$b_n J'_n(k_0 a_2) + c_n H_n^{(2)'}(k_0 a_2) = 0. \quad (190)$$

Next, it is necessary to enforce the impedance sheet boundary conditions

$$\hat{n} \times \vec{E}^+ = \hat{n} \times \vec{E}^-, \quad (191)$$

$$\hat{n} \times (\hat{n} \times \vec{E}^\pm) = -Z_s(\phi) \hat{n} \times (\vec{H}^+ - \vec{H}^-), \quad (192)$$

where  $\vec{E}^\pm = \vec{E}(a_1^\pm, \phi)$ ,  $\vec{H}^\pm = \vec{H}(a_1^\pm, \phi)$ ,  $\hat{n}$  is the unit outward normal, and  $Z_s$  is the sheet impedance which is assumed to vary with  $\phi$  in this work. Substituting (186)-(187) and (188)-(189) into (191) and (192) with  $\hat{n} = \hat{\rho}$  and applying the suitable

testing operator leads to

$$J'_n(k_0 a_1) + a_n H_n^{(2)'}(k_0 a_1) = b_n J'_n(k_0 a_1) + c_n H_n^{(2)'}(k_0 a_1), \quad (193)$$

$$\begin{aligned} \sum_{n=0}^{\infty} j \eta_0 \epsilon_n j^{-n} \left[ J'_n(k_0 a_1) + a_n H_n^{(2)'}(k_0 a_1) \right] \delta_{mn} = \\ \sum_{n=0}^{\infty} \epsilon_n j^{-n} \left[ (1 - b_n) J_n(k_0 a_1) + a_n H_n^{(2)}(k_0 a_1) - c_n H_n^{(2)}(k_0 a_1) \right] C_{mn} \end{aligned}, \quad (194)$$

where the substitution of the Fourier series expansion of the  $\phi$ -varying impedance sheet has been included. Solving (190) in terms of  $c_n$  results in

$$c_n = -b_n \frac{J'_n(k_0 a_2)}{H_n^{(2)'}(k_0 a_2)}, \quad (195)$$

which can then be substituted into (193) leading to the expression

$$b_n = \frac{J'_n(k_0 a_1) + a_n H_n^{(2)'}(k_0 a_1)}{J'_n(k_0 a_1) - \frac{J'_n(k_0 a_2)}{H_n^{(2)'}(k_0 a_2)} H_n^{(2)'}(k_0 a_1)}. \quad (196)$$

The desired  $TM^z$  scattered field expansion coefficients  $a_n$  are readily solved by substituting (195) and (196) into (194), leading with the inclusion of Wronskian and recurrence relations to (for  $m = 0, \dots, N$ )

$$\begin{aligned} - \sum_{n=0}^{\infty} \epsilon_n j^{-n} \left[ \pi k_0 \eta_0 a_1 J'_n(k_0 a_1) \delta_{mn} + \frac{2 J'_n(k_0 a_2) C_{mn}}{J'_n(k_0 a_1) H_n^{(2)'}(k_0 a_2) - J'_n(k_0 a_2) H_n^{(2)'}(k_0 a_1)} \right] = \\ \sum_{n=0}^{\infty} a_n \epsilon_n j^{-n} \left[ \pi k_0 \eta_0 a_1 H_n^{(2)'}(k_0 a_1) \delta_{mn} + \frac{2 H_n^{(2)'}(k_0 a_2) C_{mn}}{J'_n(k_0 a_1) H_n^{(2)'}(k_0 a_2) - J'_n(k_0 a_2) H_n^{(2)'}(k_0 a_1)} \right]. \end{aligned} \quad (197)$$

In expanded matrix notation, this can be practically implemented as in (137). This formulation can be verified analytically by employing a special case. If the PEC

tube within the cylinder comprised of a  $\phi$ -dependent impedance sheet is removed, then (197) should identically reduce to (168). This can be readily accomplished by allowing the imposed PEC boundary condition, as referenced by (195), to equal zero, which leads to the following

$$\sum_{n=0}^{\infty} a_n \epsilon_n j^{-n} \left[ H_n^{(2)\prime}(k_0 a_1) \delta_{mn} + \frac{2C_{mn}}{\pi \eta_0 k_0 a_1 J_n'(k_0 a_1)} \right] = \sum_{n=0}^{\infty} \epsilon_n j^{-n} J_n'(k_0 a_1) \delta_{mn}. \quad (198)$$

Thus, as the PEC tube within the cylinder comprised of a  $\phi$ -dependent impedance sheet is removed, then (197) reduces identically to (168) and grants more confidence for the solution.

### 3.4 Dielectric Filled Tapered Cylindrical Impedance Sheet

Consider a plane wave traveling along the forward  $x$  direction normally incident on a cylindrical structure that is infinite in extent along  $z$ , as illustrated in Fig. 8. The structure is comprised of an electrically-thin ( $d \ll \lambda$ ) cylindrical impedance sheet having radius  $a_1$  and an inner solid pedestal of radius  $a_2$ . The  $\phi$ -dependent high-contrast material parameters of the impedance sheet are  $\epsilon, \mu, \sigma$  and the pedestal is assumed to be comprised of simple (i.e., linear, homogeneous, isotropic) medium  $\epsilon_d, \mu_d$ . The regions  $a_2 < \rho < a_1$  and  $\rho > a_1$  are assumed to be free-space filled.

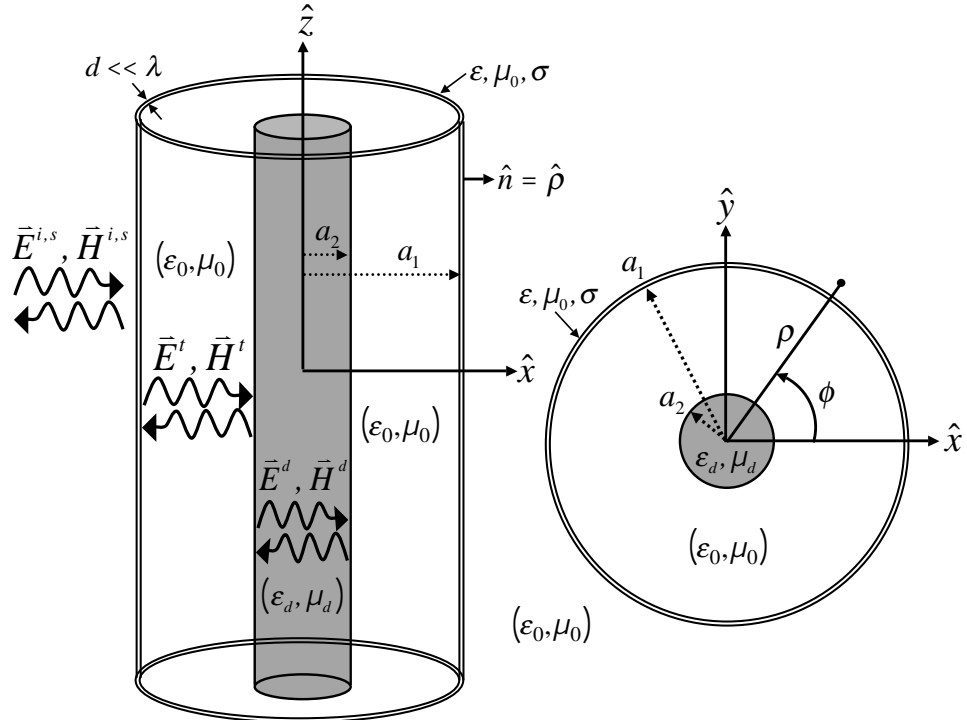


Figure 8. Side and top view of bistatic scattering from a cylinder comprised of a  $\phi$ -dependent impedance sheet wrapped about a dielectric pedestal.

Since both the scattering structure and incident excitation are  $z$ -invariant, Maxwell's equations decouple into two independent field sets,  $\text{TE}^z$  and  $\text{TM}^z$ . In addition, based on the above assumptions, an impedance sheet boundary condition may be utilized to accommodate the scattering effects of the impedance sheet. The  $z$ -invariance and

impedance sheet boundary condition implementation greatly facilitates the analytical development for the bistatic scattering width calculations, as discussed next.

### 3.4.1 $\text{TM}^z$ Polarization Development.

For  $\text{TM}^z$  polarization, the tangential electric and magnetic field (i.e., incident plus scattered) components in the region  $\rho > a_1$  can be expressed as (assuming an  $e^{j\omega t}$  time dependence)

$$E_z^{i,s}(\rho, \phi) = E_{0z}^i \sum_{n=0}^{\infty} \epsilon_n j^{-n} \left[ J_n(k_0 \rho) + a_n H_n^{(2)}(k_0 \rho) \right] \cos n\phi, \quad (199)$$

$$H_{\phi}^{i,s}(\rho, \phi) = \frac{E_{0z}^i}{j\eta_0} \sum_{n=0}^{\infty} \epsilon_n j^{-n} \left[ J'_n(k_0 \rho) + a_n H_n^{(2)'}(k_0 \rho) \right] \cos n\phi, \quad (200)$$

where  $k_0 = \omega \sqrt{\epsilon_0 \mu_0}$ ,  $\eta_0 = \sqrt{\mu_0 / \epsilon_0}$ ,  $\epsilon_n$  is the Neumann number,  $J_n$  is the Bessel function of the first kind of order  $n$ ,  $H_n^{(2)}$  is the Hankel function of the second kind of order  $n$  and the prime represents differentiation with respect to the argument. Similarly, the tangential fields in regions  $a_2 < \rho < a_1$  and  $\rho < a_2$ , respectively, may be written as

$$E_z^t(\rho, \phi) = E_{0z}^i \sum_{n=0}^{\infty} \epsilon_n j^{-n} \left[ b_n J_n(k_0 \rho) + c_n H_n^{(2)}(k_0 \rho) \right] \cos n\phi, \quad (201)$$

$$H_{\phi}^t(\rho, \phi) = \frac{E_{0z}^i}{j\eta_0} \sum_{n=0}^{\infty} \epsilon_n j^{-n} \left[ b_n J'_n(k_0 \rho) + c_n H_n^{(2)'}(k_0 \rho) \right] \cos n\phi, \quad (202)$$

$$E_z^d(\rho, \phi) = E_{0z}^i \sum_{n=0}^{\infty} d_n \epsilon_n j^{-n} J_n(k_d \rho) \cos n\phi, \quad (203)$$

$$H_{\phi}^d(\rho, \phi) = \frac{E_{0z}^i}{j\eta_d} \sum_{n=0}^{\infty} d_n \epsilon_n j^{-n} J'_n(k_d \rho) \cos n\phi, \quad (204)$$

where  $k_d = \omega \sqrt{\epsilon_d \mu_d}$  and  $\eta_d = \sqrt{\mu_d / \epsilon_d}$ .

The unknown amplitude coefficients  $a_n$ ,  $b_n$ ,  $c_n$ , and  $d_n$  are found via boundary

condition enforcement at  $\rho = a_1$  and  $\rho = a_2$ . Note, the expansion coefficient of particular relevance for bistatic scattering width calculations is  $a_n$ . Enforcing continuity of the tangential electric and magnetic fields at the pedestal interface (i.e.,  $\rho = a_2$ ) results in

$$E_{0z}^i \sum_{n=0}^{\infty} \epsilon_n j^{-n} \left[ b_n J_n(k_0 a_2) + c_n H_n^{(2)}(k_0 a_2) \right] \cos n\phi = E_{0z}^i \sum_{n=0}^{\infty} d_n \epsilon_n j^{-n} J_n(k_d a_2) \cos n\phi, \quad (205)$$

$$\frac{E_{0z}^i}{j\eta_0} \sum_{n=0}^{\infty} b_n \epsilon_n j^{-n} \left[ b_n J'_n(k_0 a_2) + c_n H_n^{(2)'}(k_0 a_2) \right] \cos n\phi = \frac{E_{0z}^i}{j\eta_d} \sum_{n=0}^{\infty} d_n \epsilon_n j^{-n} J'_n(k_d a_2) \cos n\phi, \quad (206)$$

and applying the suitable testing operator to (205) and (206) leads to the following (for  $n = 0, \dots, \infty$ )

$$b_n J_n(k_0 a_2) + c_n H_n^{(2)}(k_0 a_2) = d_n J_n(k_d a_2), \quad (207)$$

$$\eta_d \left[ b_n J'_n(k_0 a_2) + c_n H_n^{(2)'}(k_0 a_2) \right] = \eta_0 d_n J'_n(k_d a_2). \quad (208)$$

Solving (207) and (208) in terms of  $d_n$  and equating leads to the expression

$$c_n = b_n \left[ \frac{-\eta_0 J_n(k_0 a_2) J'_n(k_d a_2) + \eta_d J'_n(k_0 a_2) J_n(k_d a_2)}{\eta_0 H_n^{(2)}(k_0 a_2) J'_n(k_d a_2) - \eta_d H_n^{(2)'}(k_0 a_2) J_n(k_d a_2)} \right]. \quad (209)$$

Next, it is necessary to enforce the impedance sheet boundary conditions

$$\hat{n} \times \vec{E}^+ = \hat{n} \times \vec{E}^-, \quad (210)$$

$$\hat{n} \times (\hat{n} \times \vec{E}^\pm) = -Z_s(\phi) \hat{n} \times (\vec{H}^+ - \vec{H}^-), \quad (211)$$

where  $\vec{E}^\pm = \vec{E}(a_1^\pm, \phi)$ ,  $\vec{H}^\pm = \vec{H}(a_1^\pm, \phi)$ ,  $\hat{n}$  is the unit outward normal, and  $Z_s$  is the sheet impedance which is assumed to vary with  $\phi$  in this work. Substituting (199)-

(200) and (201)-(202) into (210) and (211) with  $\hat{n} = \hat{\rho}$  and applying the suitable testing operator leads to

$$J_n(k_0 a_1) + a_n H_n^{(2)}(k_0 a_1) = b_n J_n(k_0 a_1) + c_n H_n^{(2)}(k_0 a_1), \quad (212)$$

$$\begin{aligned} \sum_{n=0}^{\infty} j \eta_0 \epsilon_n j^{-n} \left[ J_n(k_0 a_1) + a_n H_n^{(2)}(k_0 a_1) \right] \delta_{mn} = \\ \sum_{n=0}^{\infty} \epsilon_n j^{-n} \left[ (1 - b_n) J'_n(k_0 a_1) + a_n H_n^{(2)'}(k_0 a_1) - c_n H_n^{(2)'}(k_0 a_1) \right] C_{mn} \end{aligned} \quad . \quad (213)$$

An expression for the expansion coefficient  $b_n$  in terms of  $a_n$  may be found by substituting (209) into (212) and solving to produce

$$b_n = \frac{J_n(k_0 a_1) + a_n H_n^{(2)}(k_0 a_1)}{J_n(k_0 a_1) - \left[ \frac{\eta_0 J_n(k_0 a_2) J'_n(k_d a_2) - \eta_d J'_n(k_0 a_2) J_n(k_d a_2)}{\eta_0 H_n^{(2)}(k_0 a_2) J'_n(k_d a_2) - \eta_d H_n^{(2)'}(k_0 a_2) J_n(k_d a_2)} \right] H_n^{(2)}(k_0 a_1)}. \quad (214)$$

The desired TM<sup>z</sup> scattered field expansion coefficients  $a_n$  are readily solved by substituting (209) and (214) into (213), leading to (for  $m = 0, \dots, N$ )

$$\begin{aligned} & \sum_{n=0}^{\infty} j \eta_0 \epsilon_n j^{-n} [J_n(k_0 a_1) \delta_{mn} - [J'_n(k_0 a_1) + J_n(k_0 a_1) \times \\ & \left[ \frac{\eta_0 J_n(k_0 a_2) J'_n(k_d a_2) - \eta_d J'_n(k_0 a_2) J_n(k_d a_2)}{\eta_0 H_n^{(2)}(k_0 a_2) J'_n(k_d a_2) - \eta_d H_n^{(2)'}(k_0 a_2) J_n(k_d a_2)} H_n^{(2)'}(k_0 a_1) - J'_n(k_0 a_1)} \right] C_{mn}] \\ & \left[ J_n(k_0 a_1) - \left[ \frac{\eta_0 J_n(k_0 a_2) J'_n(k_d a_2) - \eta_d J'_n(k_0 a_2) J_n(k_d a_2)}{\eta_0 H_n^{(2)}(k_0 a_2) J'_n(k_d a_2) - \eta_d H_n^{(2)'}(k_0 a_2) J_n(k_d a_2)} \right] H_n^{(2)}(k_0 a_1) \right] \\ & = \sum_{n=0}^{\infty} a_n \epsilon_n j^{-n} \left[ -j \eta_0 H_n^{(2)}(k_0 a_1) \delta_{mn} + \left[ H_n^{(2)'}(k_0 a_1) + H_n^{(2)}(k_0 a_1) \times \right. \right. \\ & \left. \left[ \frac{\eta_0 J_n(k_0 a_2) J'_n(k_d a_2) - \eta_d J'_n(k_0 a_2) J_n(k_d a_2)}{\eta_0 H_n^{(2)}(k_0 a_2) J'_n(k_d a_2) - \eta_d H_n^{(2)'}(k_0 a_2) J_n(k_d a_2)} H_n^{(2)'}(k_0 a_1) - J'_n(k_0 a_1)} \right] C_{mn} \right] \\ & \left[ J_n(k_0 a_1) - \left[ \frac{\eta_0 J_n(k_0 a_2) J'_n(k_d a_2) - \eta_d J'_n(k_0 a_2) J_n(k_d a_2)}{\eta_0 H_n^{(2)}(k_0 a_2) J'_n(k_d a_2) - \eta_d H_n^{(2)'}(k_0 a_2) J_n(k_d a_2)} \right] H_n^{(2)}(k_0 a_1) \right] \end{aligned} \quad (215)$$

In expanded matrix notation, this can be practically implemented as in (137). Also

note that the special cases of a cylindrical impedance sheet filled with free-space or a cylindrical PEC are easily obtained by letting  $\eta_d = \infty$  or  $\eta_d = 0$ , respectively.

### 3.4.2 TE<sup>z</sup> Polarization Development.

For TM<sup>z</sup> polarization, the tangential electric and magnetic field (i.e., incident plus scattered) components in the region  $\rho > a_1$  can be expressed as (assuming an  $e^{j\omega t}$  time dependence)

$$H_z^{i,s}(\rho, \phi) = H_{0z}^i \sum_{n=0}^{\infty} \epsilon_n j^{-n} \left[ J_n(k_0 \rho) + a_n H_n^{(2)}(k_0 \rho) \right] \cos n\phi, \quad (216)$$

$$E_{\phi}^{i,s}(\rho, \phi) = j H_{0z}^i \eta_0 \sum_{n=0}^{\infty} \epsilon_n j^{-n} \left[ J'_n(k_0 \rho) + a_n H_n^{(2)'}(k_0 \rho) \right] \cos n\phi, \quad (217)$$

where  $k_0 = \omega \sqrt{\epsilon_0 \mu_0}$ ,  $\eta_0 = \sqrt{\mu_0 / \epsilon_0}$ ,  $\epsilon_n$  is the Neumann number,  $J_n$  is the Bessel function of the first kind of order  $n$ ,  $H_n^{(2)}$  is the Hankel function of the second kind of order  $n$  and the prime represents differentiation with respect to the argument. Similarly, the tangential fields in regions  $a_2 < \rho < a_1$  and  $\rho < a_2$ , respectively, may be written as

$$H_z^t(\rho, \phi) = H_{0z}^i \sum_{n=0}^{\infty} \epsilon_n j^{-n} \left[ b_n J_n(k_0 \rho) + c_n H_n^{(2)}(k_0 \rho) \right] \cos n\phi, \quad (218)$$

$$E_{\phi}^t(\rho, \phi) = j H_{0z}^i \eta_0 \sum_{n=0}^{\infty} \epsilon_n j^{-n} \left[ b_n J'_n(k_0 \rho) + c_n H_n^{(2)'}(k_0 \rho) \right] \cos n\phi. \quad (219)$$

$$H_z^d(\rho, \phi) = H_{0z}^i \sum_{n=0}^{\infty} \epsilon_n j^{-n} d_n J_n(k_d \rho) \cos n\phi, \quad (220)$$

$$E_{\phi}^d(\rho, \phi) = j H_{0z}^i \eta_d \sum_{n=0}^{\infty} \epsilon_n j^{-n} d_n J'_n(k_d \rho) \cos n\phi. \quad (221)$$

where  $k_d = \omega \sqrt{\epsilon_d \mu_d}$  and  $\eta_d = \sqrt{\mu_d / \epsilon_d}$ .

The unknown amplitude coefficients  $a_n$ ,  $b_n$ ,  $c_n$ , and  $d_n$  are found via boundary

condition enforcement at  $\rho = a_1$  and  $\rho = a_2$ . Note, the expansion coefficient of particular relevance for bistatic scattering width calculations is  $a_n$ . Enforcing continuity of the tangential electric and magnetic fields at the pedestal interface (i.e.,  $\rho = a_2$ ) results in

$$jH_{0z}^i \eta_0 \sum_{n=0}^{\infty} \epsilon_n j^{-n} \left[ b_n J'_n(k_0 a_2) + c_n H_n^{(2)'}(k_0 a_2) \right] \cos n\phi = , \quad (222)$$

$$jH_{0z}^i \eta_d \sum_{n=0}^{\infty} \epsilon_n j^{-n} d_n J'_n(k_d a_2) \cos n\phi = , \quad (223)$$

$$H_{0z}^i \sum_{n=0}^{\infty} \epsilon_n j^{-n} \left[ b_n J_n(k_0 a_2) + c_n H_n^{(2)}(k_0 a_2) \right] \cos n\phi = ,$$

and applying the suitable testing operator to (222) and (223) leads to the following (for  $n = 0, \dots, \infty$ )

$$\eta_0 \left[ b_n J'_n(k_0 a_2) + c_n H_n^{(2)'}(k_0 a_2) \right] = \eta_d d_n J'_n(k_d a_2), \quad (224)$$

$$b_n J_n(k_0 a_2) + c_n H_n^{(2)}(k_0 a_2) = d_n J_n(k_d a_2). \quad (225)$$

Solving (224) and (225) in terms of  $d_n$  and equating leads to the expression

$$c_n = -b_n \left[ \frac{\eta_0 J'_n(k_0 a_2) J_n(k_d a_2) - \eta_d J_n(k_0 a_2) J'_n(k_d a_2)}{\eta_0 H_n^{(2)'}(k_0 a_2) J_n(k_d a_2) - \eta_d H_n^{(2)}(k_0 a_2) J'_n(k_d a_2)} \right]. \quad (226)$$

Next, it is necessary to enforce the impedance sheet boundary conditions

$$\hat{n} \times \vec{E}^+ = \hat{n} \times \vec{E}^-, \quad (227)$$

$$\hat{n} \times (\hat{n} \times \vec{E}^\pm) = -Z_s(\phi) \hat{n} \times (\vec{H}^+ - \vec{H}^-), \quad (228)$$

where  $\vec{E}^\pm = \vec{E}(a_1^\pm, \phi)$ ,  $\vec{H}^\pm = \vec{H}(a_1^\pm, \phi)$ ,  $\hat{n}$  is the unit outward normal, and  $Z_s$  is the

sheet impedance which is assumed to vary with  $\phi$  in this work. Substituting (216)-(217) and (218)-(219) into (227) and (228) with  $\hat{n} = \hat{\rho}$  and applying the suitable testing operator leads to

$$J'_n(k_0a_1) + a_n H_n^{(2)'}(k_0a_1) = b_n J'_n(k_0a_1) + c_n H_n^{(2)'}(k_0a_1), \quad (229)$$

$$\begin{aligned} \sum_{n=0}^{\infty} j\eta_0\epsilon_n j^{-n} \left[ J'_n(k_0a_1) + a_n H_n^{(2)'}(k_0a_1) \right] \delta_{mn} = \\ - \sum_{n=0}^{\infty} \epsilon_n j^{-n} \left[ (1 - b_n) J_n(k_0a_1) + a_n H_n^{(2)}(k_0a_1) - c_n H_n^{(2)}(k_0a_1) \right] C_{mn} \end{aligned} \quad . \quad (230)$$

An expression for the expansion coefficient  $b_n$  in terms of  $a_n$  may be found by substituting (226) into (229) and solving to produce

$$b_n = \frac{J'_n(k_0a_1) + a_n H_n^{(2)'}(k_0a_1)}{J'_n(k_0a_1) - \left[ \frac{\eta_0 J'_n(k_0a_2) J_n(k_da_2) - \eta_d J_n(k_0a_2) J'_n(k_da_2)}{\eta_0 H_n^{(2)'}(k_0a_2) J_n(k_da_2) - \eta_d H_n^{(2)}(k_0a_2) J'_n(k_da_2)} \right] H_n^{(2)'}(k_0a_1)}. \quad (231)$$

The desired  $\text{TM}^z$  scattered field expansion coefficients  $a_n$  are readily solved by substituting (226) and (231) into (230), leading to (for  $m = 0, \dots, N$ )

$$\begin{aligned} & - \sum_{n=0}^{\infty} j\eta_0\epsilon_n j^{-n} [J'_n(k_0a_1) \delta_{mn} - [J_n(k_0a_1) + J'_n(k_0a_1) \times \\ & \left[ \frac{\eta_0 J'_n(k_0a_2) J_n(k_da_2) - \eta_d J_n(k_0a_2) J'_n(k_da_2)}{\eta_0 H_n^{(2)'}(k_0a_2) J_n(k_da_2) - \eta_d H_n^{(2)}(k_0a_2) J'_n(k_da_2)} H_n^{(2)}(k_0a_1) - J_n(k_0a_1) \right] H_n^{(2)'}(k_0a_1) \times \\ & \left[ J'_n(k_0a_1) - \left[ \frac{\eta_0 J'_n(k_0a_2) J_n(k_da_2) - \eta_d J_n(k_0a_2) J'_n(k_da_2)}{\eta_0 H_n^{(2)'}(k_0a_2) J_n(k_da_2) - \eta_d H_n^{(2)}(k_0a_2) J'_n(k_da_2)} \right] H_n^{(2)'}(k_0a_1) \right] C_{mn}] \\ & = \sum_{n=0}^{\infty} a_n \epsilon_n j^{-n} \left[ j\eta_0 H_n^{(2)'}(k_0a_1) \delta_{mn} + \left[ H_n^{(2)}(k_0a_1) + H_n^{(2)'}(k_0a_1) \times \right. \right. \\ & \left. \left[ \frac{\eta_0 J'_n(k_0a_2) J_n(k_da_2) - \eta_d J_n(k_0a_2) J'_n(k_da_2)}{\eta_0 H_n^{(2)'}(k_0a_2) J_n(k_da_2) - \eta_d H_n^{(2)}(k_0a_2) J'_n(k_da_2)} H_n^{(2)}(k_0a_1) - J_n(k_0a_1) \right] H_n^{(2)'}(k_0a_1) \times \\ & \left. \left[ J'_n(k_0a_1) - \left[ \frac{\eta_0 J'_n(k_0a_2) J_n(k_da_2) - \eta_d J_n(k_0a_2) J'_n(k_da_2)}{\eta_0 H_n^{(2)'}(k_0a_2) J_n(k_da_2) - \eta_d H_n^{(2)}(k_0a_2) J'_n(k_da_2)} \right] H_n^{(2)'}(k_0a_1) \right] C_{mn} \right] \end{aligned} \quad (232)$$

In expanded matrix notation, this can be practically implemented as in (137). Also note that the special cases of a cylindrical impedance sheet filled with free-space or a cylindrical PEC are easily obtained by letting  $\eta_d = \infty$  or  $\eta_d = 0$ , respectively.

## IV. Experimental Results

In the previous chapter, the scattered field expansion coefficient development of  $\text{TM}^z$  and  $\text{TE}^z$  polarizations for a cylinder comprised of a  $\phi$ -dependent impedance sheet were derived. This relied on general impedance sheet boundary conditions in addition to a Fourier series representation of the impedance sheet distribution, with the utilization of Wronskian and recurrence relations, to produce a computationally efficient matrix solution for the scattered field expansion coefficients  $a_n$ . The scattering coefficients  $a_n$  can now be included in the expression for a two-dimensional scattering width, allowing for the scattering patterns of arbitrary diameter cylinder impedance sheet distributions. The ability to adapt sheet impedances to effectively control the overall nulls in the bistatic scattering pattern will be demonstrated, with practically implemented impedance characteristics. Lastly, a novel rectangular X-band waveguide system will be utilized to characterize the electromagnetic properties of the  $\phi$ -dependent impedance sheet.

### 4.1 Bistatic Scattering

In order to obtain a meaningful representation of the scattered field, the two-dimensional scattering width will be utilized. This will allow for insight on how the impedance distribution about the cylinder affects the scattering pattern. The bistatic scattering width may be computed via

$$\sigma_{2D} = \lim_{\rho \rightarrow \infty} \left[ 2\pi\rho \frac{|E^s(\rho, \phi)|^2}{|E^i(\rho, \phi)|^2} \right], \quad (233)$$

which upon using the asymptotic expansion for the scattered field becomes (normalized with respect to wavelength)

$$\frac{\sigma_{2D}}{\lambda} = \frac{2}{\pi} \left| \sum_{n=0}^N \epsilon_n a_n \cos n\phi \right|^2. \quad (234)$$

As previously mentioned, the number of terms  $N$  in (234) is chosen such that convergence is reached to within a tolerance of  $1 \times 10^{-7}$ . Calculation of the expansion coefficients  $a_n$  and corresponding bistatic scattering width for various impedance sheet distributions is demonstrated next.

In order to demonstrate the effect that impedance sheet tapering has on the bistatic scattering pattern (when compared to a uniform sheet), two scattering scenarios are investigated here. The two cases involve a tapered impedance sheet filled with a dielectric and PEC pedestal, respectively. Note, as discussed in the theory, an  $x$ -directed normally-incident plane wave excitation is assumed.

#### 4.1.1 Dielectric pedestal results.

Consider a non-magnetic polystyrene pedestal having permittivity  $\epsilon_d = 1.5\epsilon_0$  and radius  $a_1 = \lambda$  surface-wrapped (i.e.,  $a_2 = a_1$ ) with the tapered impedance sheet distribution  $Z_s(\phi)$  shown in Figure 9. This distribution represents a physically-realizable sinusoidal impedance taper from 0 to  $1000-j200 \Omega$  consisting of a single period about the cylinder. As will be shown below, this relatively simple complex impedance sheet distribution can effectively introduce specific nulls in the bistatic scattering width unattainable with a constant impedance sheet and allows the null positions to be readily controlled.

The bistatic scattering widths illustrated in Figure 10 depict the effects of the  $\text{TM}^z$  polarization. At its initial setup state, the single sinusoid impedance sheet distribution introduces particular nulls near 60 and 100 degrees. These nulls are non-

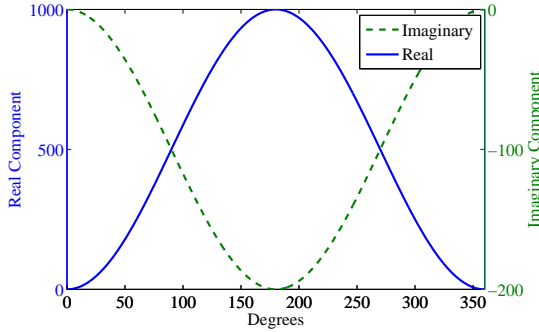


**Figure 9. Single sinusoid  $\phi$ -dependent impedance sheet distribution.**

trivial, with a two-dimensional scattering width improvement of about 17 dB and 14 dB, respectively. Rotating the pedestal by 23.4 degrees deepens the null at 60 degrees to a reduction of 37 dB while maintaining the 100 degree null at about 12 dB. Then, rotating the pedestal by 90 degrees effectively repositions the two nulls, resulting in two-dimensional scattering width improvements at 25, 70, 110, and 150 degrees with respective reductions of about 10 dB, 9.5 dB, 9 dB, and 7.5 dB. Overall, the bistatic scattering widths presented Figure 10 demonstrate three key features of tapered over uniform impedance sheet. It shows how a tapered impedance sheet not only introduces controllable and particular nulls in the bistatic scattering widths, but the ability to significantly increase the reduction amount at certain angles. These effects will be seen again in the remaining analysis.

Figure 11 illustrates the bistatic scattering widths of  $TE^z$  polarization. At its initial setup state, the single sinusoid impedance sheet distribution introduces a broad null centered at 60 degrees and a particular null near 120 degrees. These nulls are non-incidental, with the broad null reducing the two-dimensional scattering width by at least 10 dB from about 45 to 75 degrees, with a maximum reduction of 18 dB. Meanwhile, the particular null at 120 degrees improves the bistatic scattering width by 16 dB. Then, rotating the pedestal by 90 degrees effectively repositions the nulls

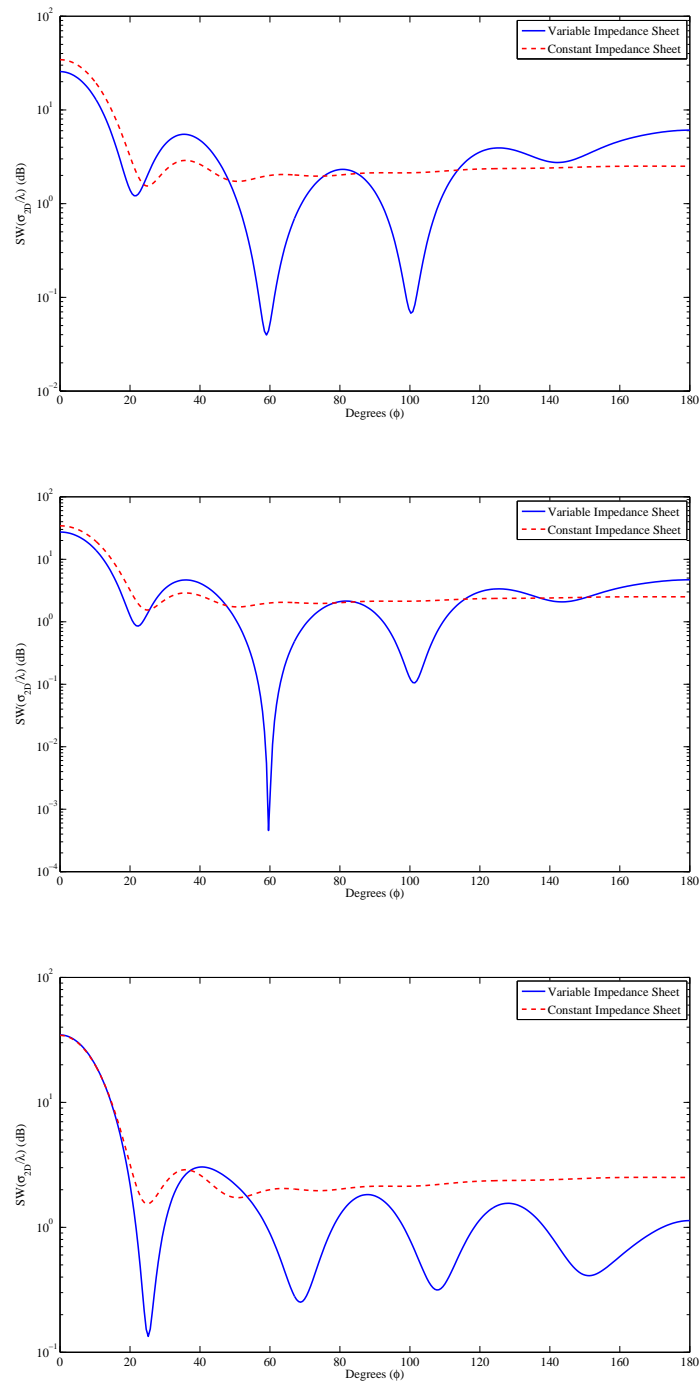


**Figure 10. 2D Bistatic Scattering Width of  $\text{TM}^z$  polarization (Top: 0 degrees, Middle: 23.4 degrees, Bottom: 90 degrees) for the  $\phi$ -dependent impedance sheet filled with a polystyrene pedestal.**

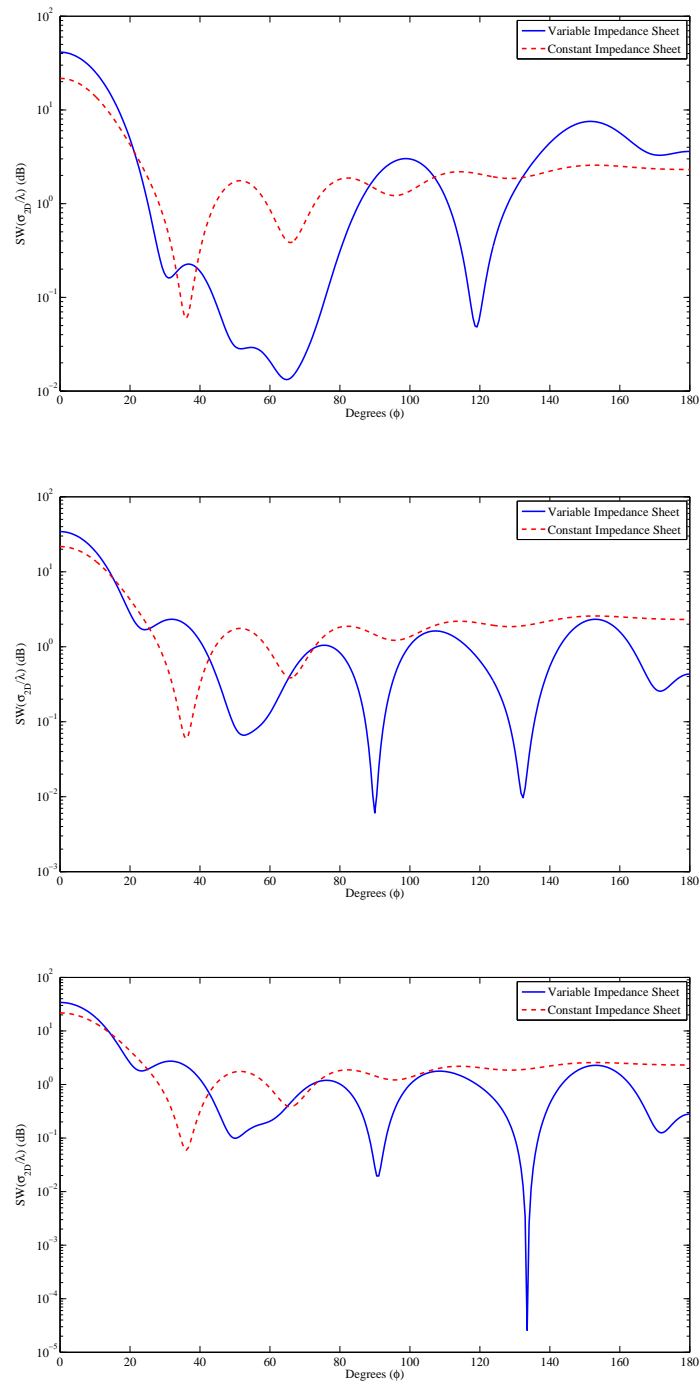


**Figure 11. 2D Bistatic Scattering Width of  $\text{TE}^z$  polarization (Top: 0 degrees, Middle: 90 degrees, Bottom: 104.4 degrees) for the  $\phi$ -dependent impedance sheet filled with a polystyrene pedestal.**

to about 90 and 135 degrees, with corresponding reductions of 24 dB and 21 dB. Additionally, at this rotation a 14 dB null remains at 50 degrees while a 9 dB null at 170 degrees is introduced. Again, rotating the pedestal by 104.4 degrees deepens the null at 130 degrees to about 48 dB while conserving the remaining reductions of about 11 dB, 20 dB, and 11 dB for the 50, 90, and 170 degree nulls. As previously noted, the bistatic scattering widths presented Figure 11 demonstrate how a tapered impedance sheet not only introduces controllable and particular nulls in the bistatic scattering widths, but the ability to significantly increase the reduction amount at certain angles.

#### 4.1.2 PEC pedestal results.

Consider a PEC pedestal having a radius  $a_1 = \lambda$  surface gap-wrapped (i.e.,  $a_1 - a_2 = .25\lambda$ ) with the tapered impedance sheet distribution  $Z_s(\phi)$  shown in Figure 9. As will be shown below for this more obtrusive pedestal, the relatively simple, physically-realizable complex impedance sheet distribution can effectively introduce specific nulls in the bistatic scattering width unattainable with a constant impedance sheet and allows the null positions to be readily controlled.

The bistatic scattering widths illustrated in Figure 12 depict the  $\text{TM}^z$  polarization. At its initial setup state the single sinusoid impedance sheet distribution introduces an effective null near 55 degrees. This null improves the two-dimensional scattering width by about 16 dB. As before, rotating the pedestal by 36.0 degrees deepens the null at 55 degrees to a non-trivial amount of 40 dB. Then, rotating the pedestal by 108.0 degrees effectively repositions the null, resulting in improvements ranging from about 80 to 180 degrees. The reduction amount increases from 5 dB at 80 degrees to 40 dB at 180 degrees, with a maximum reduction of 46 dB at 170 degrees. Again, the bistatic scattering widths presented Figure 12 demonstrate how a tapered impedance

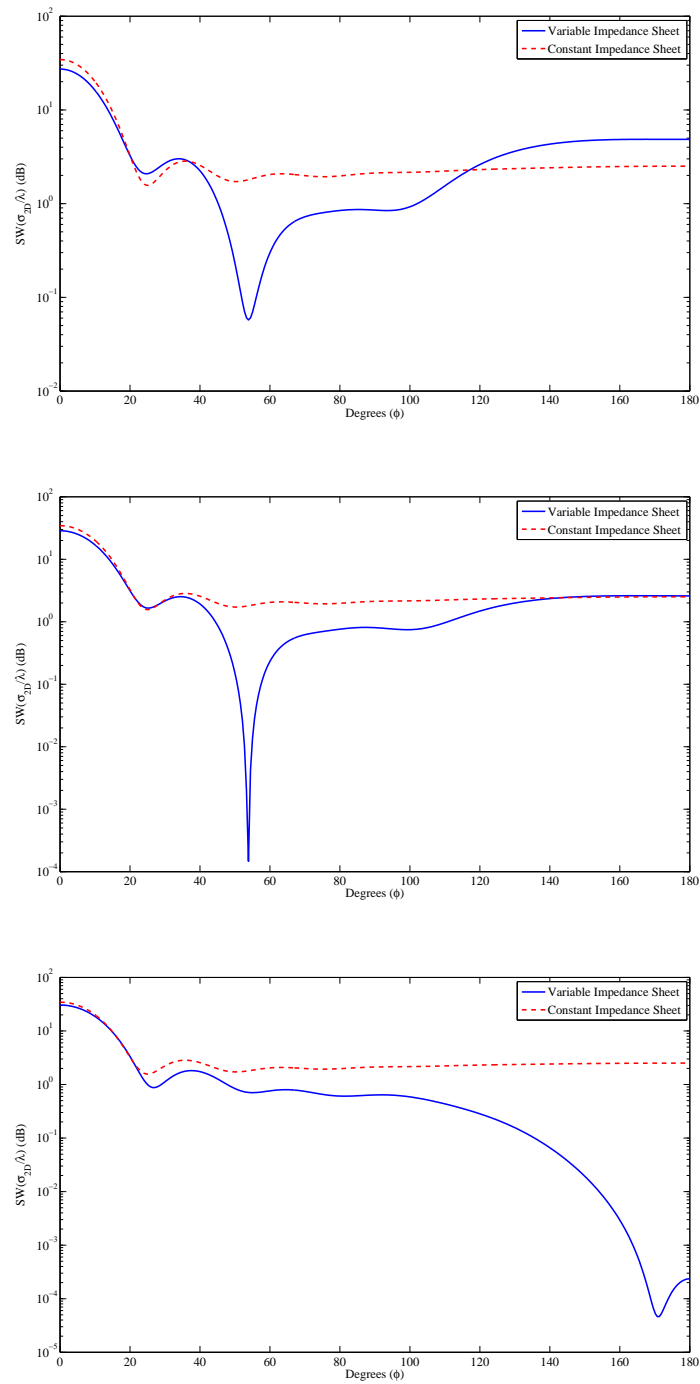


**Figure 12. 2D Bistatic Scattering Width of  $\text{TM}^z$  polarization (Top: 0 degrees, Middle: 36.0 degrees, Bottom: 108.0 degrees) for the  $\phi$ -dependent impedance sheet partially filled with a PEC pedestal.**

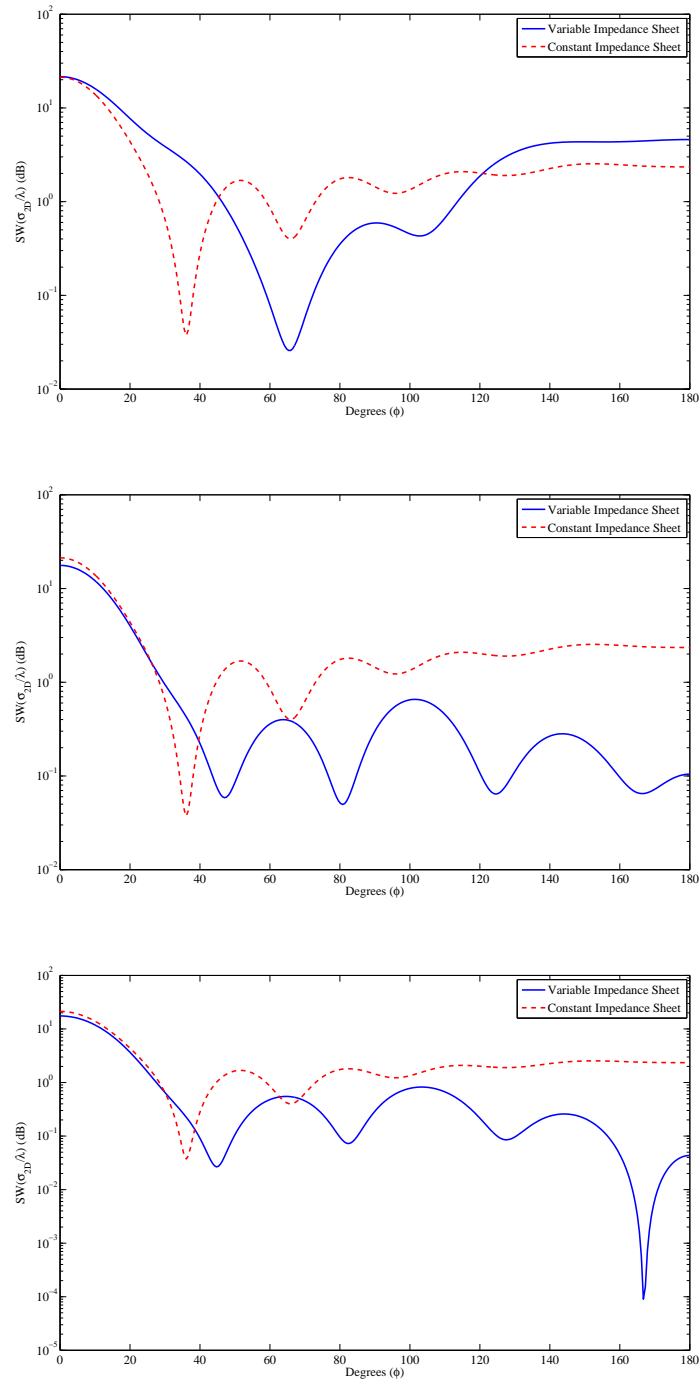


**Figure 13. 2D Bistatic Scattering Width of  $\text{TE}^z$  polarization (Top: 0 degrees, Middle: 90 degrees, Bottom: 104.4 degrees) for the  $\phi$ -dependent impedance sheet partially filled with a PEC pedestal.**

sheet not only introduces controllable and particular nulls in the bistatic scattering widths, but the ability to significantly increase the reduction amount at certain angles.

Figure 13 illustrates the bistatic scattering widths of  $TE^z$  polarization. At its initial setup state the single sinusoid impedance sheet distribution introduces a general decrease in the bistatic scattering width by at least 5 dB from 50 to 100 degrees, with more substantial null of 12 dB centered about 65 degrees. These reductions, however, come as a trade-off given that there actually exists an increase in the bistatic scattering width from 20 to 40 degrees. Rotating the pedestal by 90 degrees effectively repositions the previous null and introduces additional nulls at 45, 80, 125, and 165 degrees, with corresponding reductions of 14 dB, 15 dB, 14 dB, and 15 dB. Additionally, at this rotation a general improvement in the bistatic scattering width exists from about 70 to 180 degrees. Again, rotating the pedestal by 104.4 degrees deepens the null at 165 degrees to about 42 dB while conserving the remaining reductions of about 18 dB, 13 dB, and 12 dB for the 45, 80, and 125 degree nulls. As with every figure before, the bistatic scattering widths presented Figure 13 demonstrate how a tapered impedance sheet not only introduces controllable and particular nulls in the bistatic scattering widths, but the ability to significantly increase the reduction amount at certain angles.

It is important to note that these distributions can be approximately realized with current fabrication techniques, as developed in [2]. The employed technique utilizes a constant impedance sheet, typically a Kapton KC film, and manipulates the effective-medium properties via a method of printing metallic squares and burning out squares of various dimensions and spatial variations. Though the presented impedance sheet distributions are physically realizable, the fabrication process itself has some prohibitive limitations for this research. First, in order to validate these 2D bistatic scattering width patterns, a 2D-to-3D conversion must be employed (in the absence

of an available industry computer code), as shown below

$$\sigma_{3D} \approx \frac{2L^2}{\lambda} \sigma_{2D}, \quad (235)$$

where  $L$  is total axial length of the cylinder such that  $L \gg \lambda$ . Thus, for X-band frequencies the cylinder must have a minimum length of 36.5 cm, as determined by the minimum frequency of 8.2 GHz. The maximum area that can currently be fabricated,

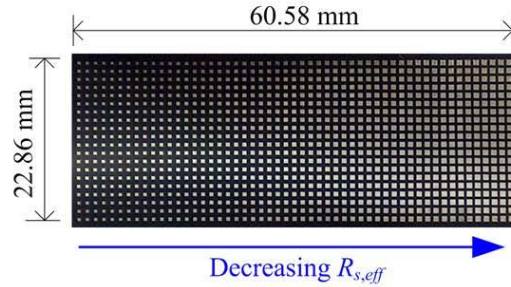


**Figure 14. Example of a tapered impedance sheet based on a Kapton KC film substrate.**

however, is about 10 cm sq. Increasing the desired frequency range to circumvent this limitation is not viable either given the physical limits in printing microscopic metallic squares and burning out microscopic squares in the Kapton KC film. Despite this current limitation, a viable electromagnetic characterization technique can still be utilized to help verify the currently realizable physical samples.

## 4.2 Electromagnetic Characterization Process

In order to mitigate the inhomogeneity of the tapered R-cards, a novel electromagnetic characterization technique must be adopted. This specialized technique employs a stepped flange waveguide and modal analysis approach in order to approximately treat the tapered R-card as a piecewise homogeneous material. The main objective is to focus the incident electromagnetic energy into a smaller sample area of the tapered R-cards suspended between two flanges, as shown below.

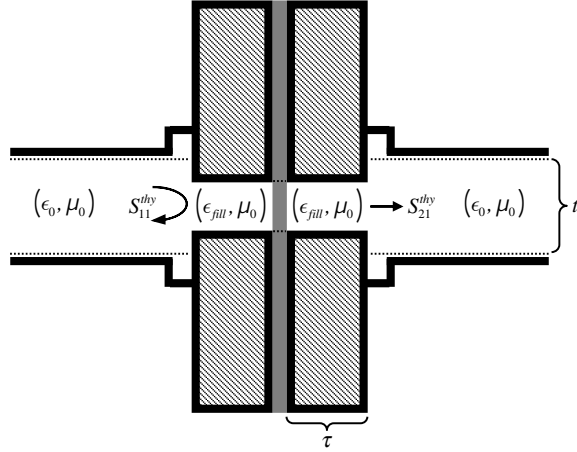


**Figure 15.** Theoretical stepped flange waveguide setup where the gray substance represents the tapered R-card.

This process ultimately produces the theoretical scattering parameters ( $S_{11}^{thy}$ ,  $S_{21}^{thy}$ ) for the entire stepped flange waveguide setup. With theoretical values for the complex permittivity and permeability of the R-card embedded within the derived scattering parameters, an iterative root search must then be implemented to solve for the actual values for the R-card's complex permittivity and permeability. This is accomplished via the Newton-Raphson root search which solves for the following relations

$$\begin{aligned} S_{11}^{thy}(\omega, \epsilon) - S_{11}^{exp}(\omega) &< tol \\ S_{21}^{thy}(\omega, \epsilon) - S_{21}^{exp}(\omega) &< tol \end{aligned} \quad (236)$$

where  $tol = 10^{-7}$ . With the modal analysis technique the fields in each region of the stepped waveguide setup are expanded, followed by satisfying the interfacial boundary conditions and applying an appropriate integral testing operator. The introduction of the stepped flanges disrupt the waveguide wall surface currents and excite higher-order modes. These higher-order modes, though accommodated by the mode-matching technique, evanesce within the waveguide. This can lead to insufficient transmitted energy received by the vector network analyzer to accurately determine the complex permittivity of the sample R-card. Two solutions to this problem are presented. The

first method is to fill the stepped flange waveguide with a low loss dielectric ( $\epsilon_{fill}, \mu_0$ ) in order to couple more energy through the waveguide. The second is to simply make the stepped flanges less thick ( $\tau$ ), such that the energy has less opportunity to evanesce.

The ultimate objective is to determine the R-card sheet impedance. This can be readily accomplished via an AC expression relating the effective sheet impedance  $Z_{\text{eff}}$  and the extracted complex permittivity  $\epsilon_{\text{eff}}$  [3]

$$Z_{\text{eff}} = \frac{1}{\sigma_{\text{eff}}\tau} = \frac{1}{j\omega(\epsilon_{\text{eff}} - \epsilon_0)} = -\frac{j\eta_0 c}{\omega\tau(\epsilon_r^{\text{eff}} - 1)}, \quad (237)$$

where  $\sigma_{\text{eff}}$  is the effective complex conductivity,  $\tau$  is the sheet thickness,  $\omega$  is the angular excitation frequency,  $c$  is the speed of light, and  $\epsilon_r^{\text{eff}} = \epsilon_{\text{eff}}/\epsilon_0 = (\epsilon + \sigma/j\omega)/\epsilon_0$  is the relative effective complex permittivity.

#### 4.2.1 Experimental Setup.

All measurements were conducted with a HP8510C Vector Network Analyzer connected to a WR90 waveguide setup, where the WR represents “waveguide rectangular” and 90 indicates the aperture width of 0.90 inches. The full X-band frequency range of 8.2 GHz to 12.4 GHz was used along with employing the industry standard TRL calibration technique. Furthermore, all measurements are accompanied by a differential error analysis focusing on the uncertainty of the plate flange dimensions and R-card thickness[22].

Without being able to obtain a sample tapered R-card, a proof of concept was conducted with readily available uniform R-cards of various values. Validation of the electromagnetic characterization technique required the use of several variations amongst the aperture size of the stepped flange, the thickness of the flange, and the R-card resistivity. Consequently, each particular test setup variant conducted tests with

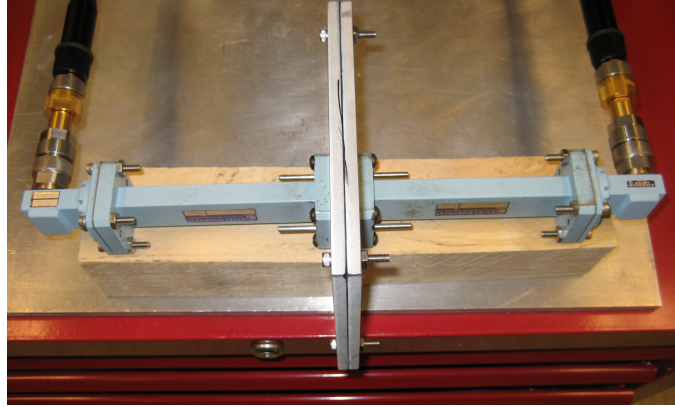


**Figure 16. Experimental setup of the stepped waveguide and flanges.**

three different R-cards of about  $400 \Omega/sq$ ,  $900 \Omega/sq$ , and  $2000 \Omega/sq$  to demonstrate usefulness across a range of impedances. The setup variants themselves consisted of plate flanges (6.47 mm thick) and sheet flanges (.673 mm). Furthermore, both the plate and sheet flanges had three more aperture size variants of 0.1 inches, 0.2 inches, and 0.3 inches. Each variant, in turn, was ultimately compared to the results from a full X-band flange ( $t = 0.9$  inches). With the full X-band flange only the dominant  $TE_{10}$  mode would be excited, acting as an ideal baseline measurement.

#### 4.2.2 0.1 inch Aperture Flange.

The 0.1 inch aperture flange represented the smallest taper to be experimented upon and performed the worse of the three aperture widths. With such a small aperture very little energy is transmitted through the sample, with nearly all the energy being reflected back, as illustrated in Figure 18. At this width, both the empty and filled plate flanges failed to allow sufficient energy to pass through, resulting in the  $S_{21}$  parameter falling completely into the noise floor. The sheet flange, however, allowed sufficient energy to be transmitted through the sample to measure above the noise floor.



**Figure 17. Experimental setup variant of the 0.1 inch plates and sheets.**

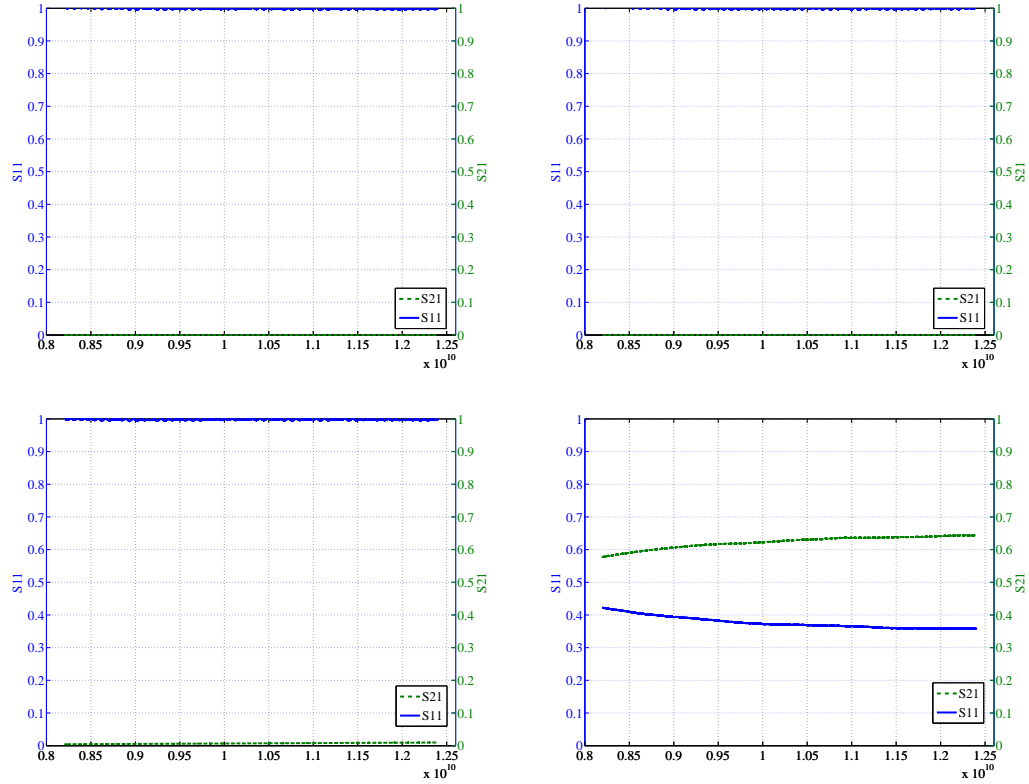


**Figure 18. Experimental scattering parameters for the 0.1 inch aperture flange (top-left: empty plate, top-right: filled plate, bottom-left: sheet, bottom-right: X-band).**

Due to the excessive noise present in the scattering parameters from the 0.1 inch aperture flange plates, both filled and empty, it is impossible to employ the numerical

Newton-Raphson root search technique. The root search can, however, be applied to the 0.1 inch sheet flange scattering parameters, to extract the complex impedance values in an erratic fashion. These extracted impedance values fail to converge to the baseline X-band impedance values, as evidenced by Figures 19, 20, and 21.

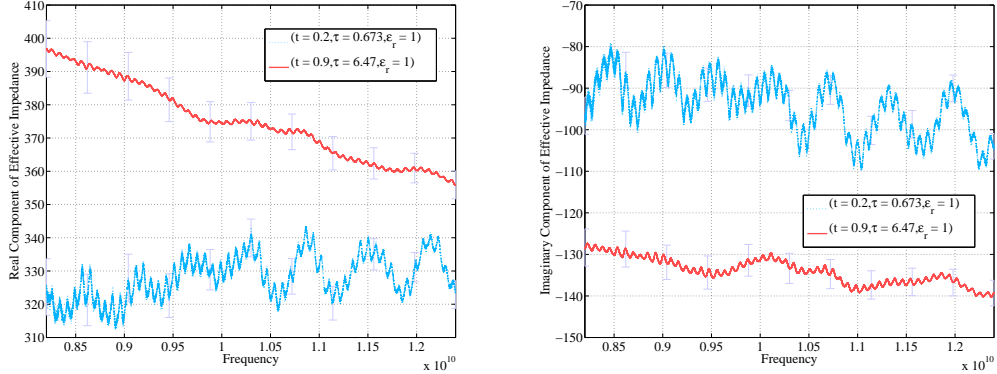


**Figure 19. Real and imaginary components of the effective impedance for the 400 ohm R-card with a 0.1 inch aperture flange.**

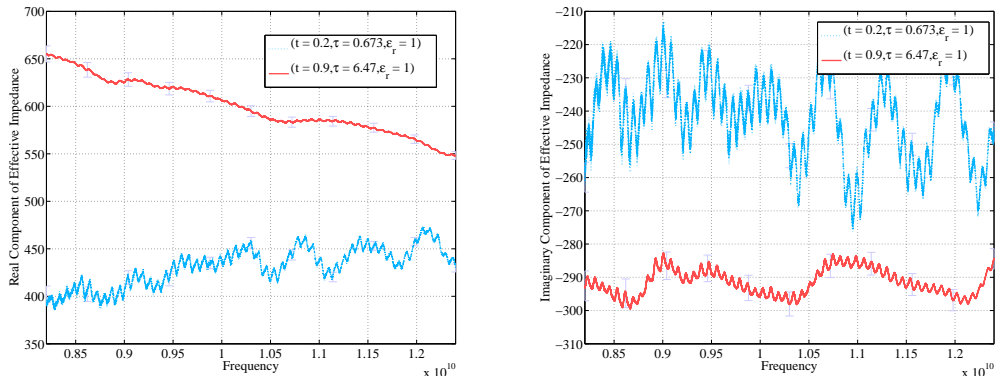


**Figure 20. Real and imaginary components of the effective impedance for the 900 ohm R-card with a 0.1 inch aperture flange.**

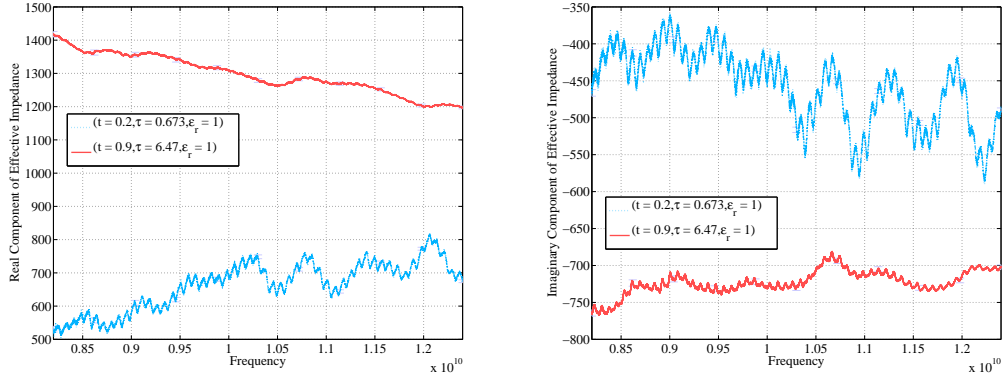


**Figure 21. Real and imaginary components of the effective impedance for the 2000 ohm R-card with a 0.1 inch aperture flange.**

A summary of the maximum difference between the 0.1 inch sheet flange and full X-band extracted complex impedance values is shown below.

**Table 1. Summary of Maximum Complex Impedance Error from the 0.1 inch Sheet Flange**

R-card	Real Component	Imaginary Component
400 $\Omega$	27.5%	11.4%
900 $\Omega$	57.0%	25.0%
2000 $\Omega$	137.5%	52.7%

For the sheet flange measurements, the relatively minor noise present in the S21 parameters with magnitudes on the order of  $10^{-4}$  prohibit the root search technique from effectively extracting the correct complex impedance values.

#### 4.2.3 0.2 inch Aperture Flange.

The 0.2 inch aperture flange represented the second taper to be experimented upon and performed with mixed success. For all flange variants sufficient energy passed through the sample to measure above the noise floor, as illustrated in Figure 23. In this case, the experimentally measured S21 magnitudes for the aperture flange plates, both filled and empty, contain relatively significant fluctuations due to noise. The sheet flange S21 magnitudes, though, are seen to be free of any such fluctuations.

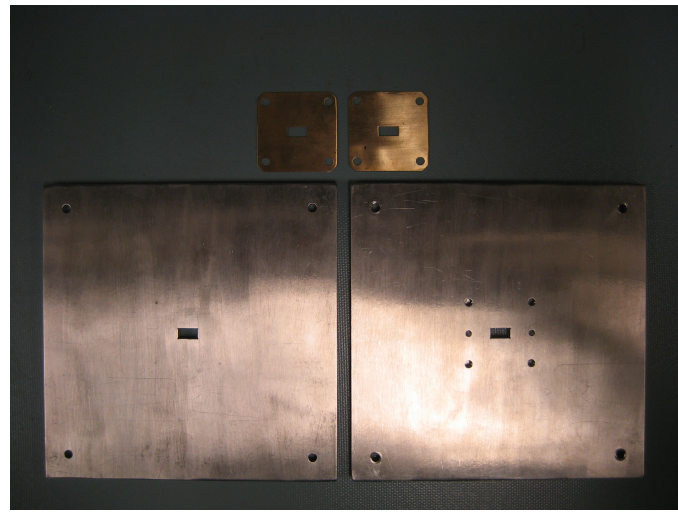


Figure 22. Experimental setup variant of the 0.2 inch plates and sheets.

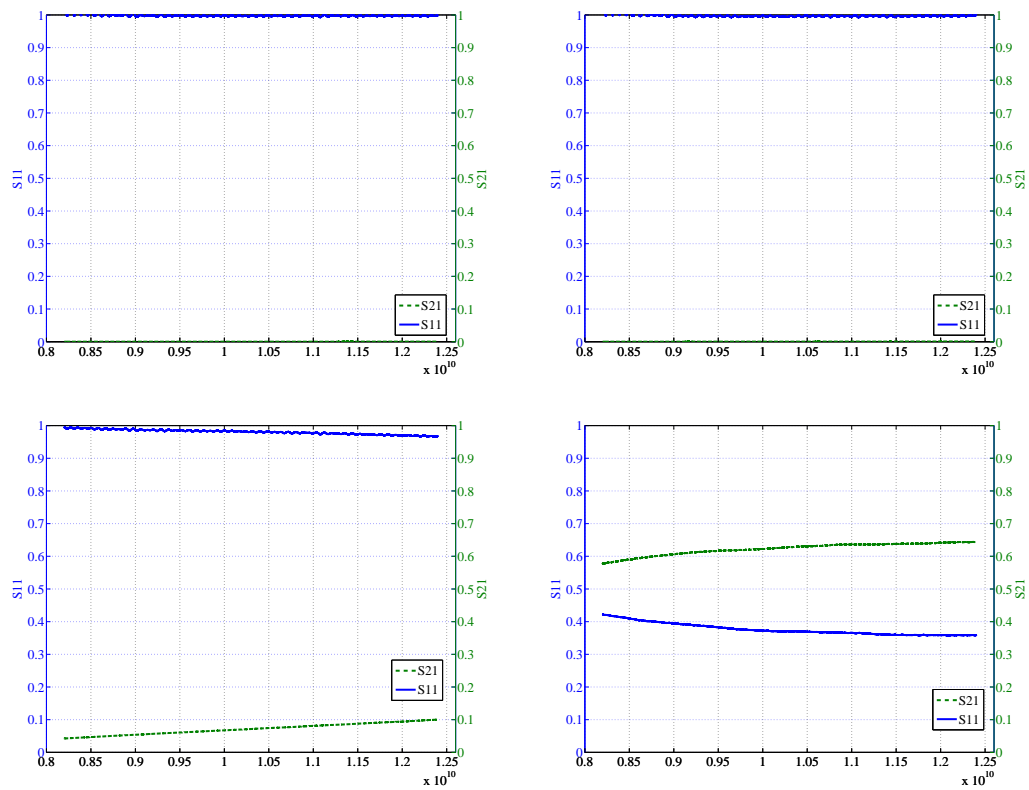
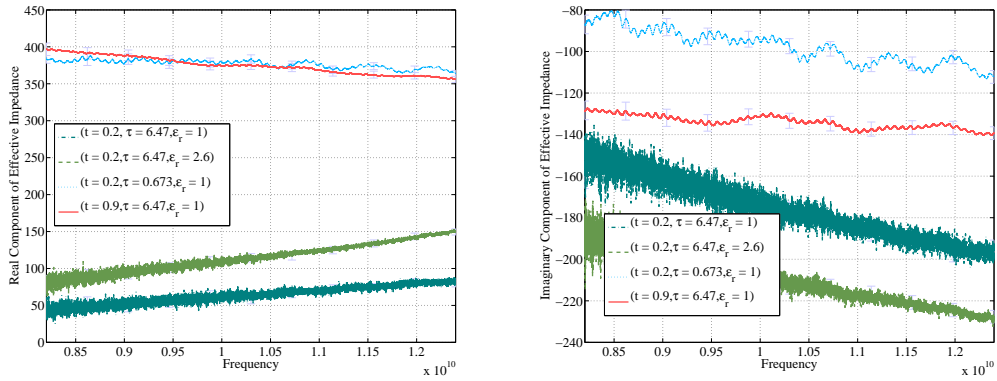


Figure 23. Experimental scattering parameters for the 0.2 inch aperture flange (top-left: empty plate, top-right: filled plate, bottom-left: sheet, bottom-right: X-band).

Also, close examination upon the S21 magnitude of the empty to filled plate flange reveals that the included plexiglass allows about 10 times more energy to transmit through the sample.

Due to the noise present in the scattering parameters from the 0.2 inch aperture flange plates, both filled and empty, the root search technique performs unsuccessfully, as previously experienced by the 0.1 inch sheet flange. Still, the dielectric filled plate flange shows an improvement in the extracted complex permittivity over the empty plate flange, due to the additional energy transmitted through the sample. The 0.2 inch sheet flange S21 parameters, absent of the noise fluctuations, effectively produces extracted complex permittivity values that converge to the baseline X-band permittivity values, as evidenced by Figures 24, 25, and 26.



**Figure 24.** Real and imaginary components of the effective impedance for the 400 ohm R-card with a 0.2 inch aperture flange.

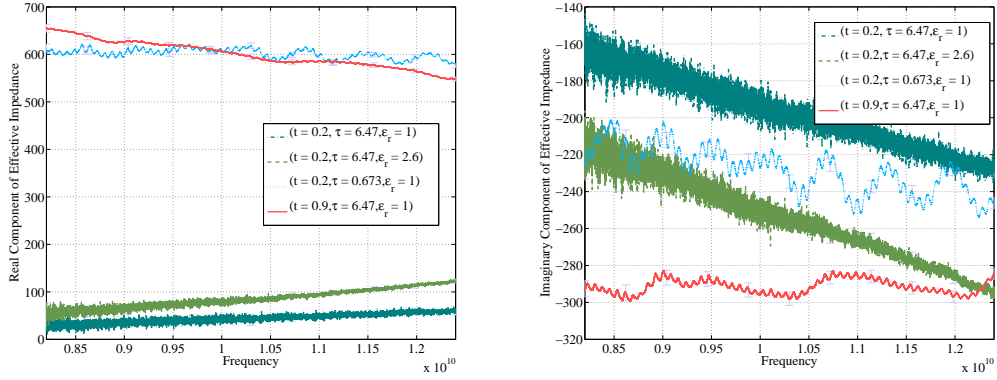


**Figure 25. Real and imaginary components of the effective impedance for the 900 ohm R-card with a 0.2 inch aperture flange.**

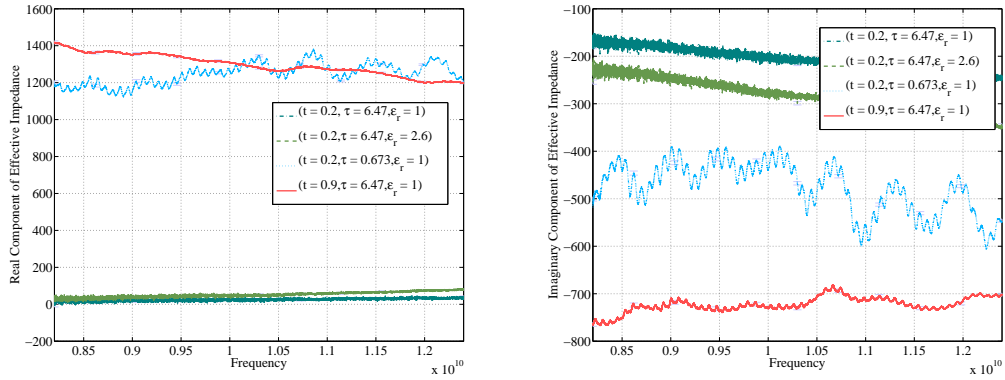


**Figure 26. Real and imaginary components of the effective impedance for the 2000 ohm R-card with a 0.2 inch aperture flange.**

A summary of the maximum difference between the 0.2 inch empty plate, filled plate, and sheet flange to the full X-band extracted complex impedance values is shown below.

**Table 2. Summary of Maximum Complex Impedance Error from the 0.2 inch Empty Plate Flange**

R-card	Real Component	Imaginary Component
400 $\Omega$	77.6%	248.2%
900 $\Omega$	205.7%	403.2%
2000 $\Omega$	553.8%	890.5%

For the empty and filled plate flange S21 parameters, the noise present in the measurements prohibit the root search technique from effectively extracting the correct

**Table 3. Summary of Maximum Complex Impedance Error from the 0.2 inch Filled Plate Flange**

R-card	Real Component	Imaginary Component
400 $\Omega$	51.9%	173.0%
900 $\Omega$	128.4%	293.5%
2000 $\Omega$	403.4%	617.4%

**Table 4. Summary of Maximum Complex Impedance Error from the 0.2 inch Sheet Flange**

R-card	Real Component	Imaginary Component
400 $\Omega$	6.5%	11.7%
900 $\Omega$	11.9%	12.1%
2000 $\Omega$	27.5%	23.8%

complex impedance values. The sheet flange S21 parameters, without any significant noise, produce fairly accurate real impedance values for each R-card sample. The imaginary component, on the other hand, tends to converge to the incorrect value as it is significantly more sensitive to slight fluctuations in the measurements.

#### 4.2.4 0.3 inch Aperture Flange.

The 0.3 inch aperture flange represented the largest taper to be experimented upon and performed with the most success.



**Figure 27. Experimental setup variant of the 0.3 inch plates and sheets.**

For all flange variants, with the exception of the empty plate, sufficient energy passed through the sample to measure above the noise floor, as illustrated in Figure 28. In this case, none of the experimentally measured S21 magnitudes appear to contain significant fluctuations due to noise. As previously seen, comparing the S21 magnitude of the empty to filled plate flange reveals that the included plexiglass allows about 10 times more energy to transmit through the sample.

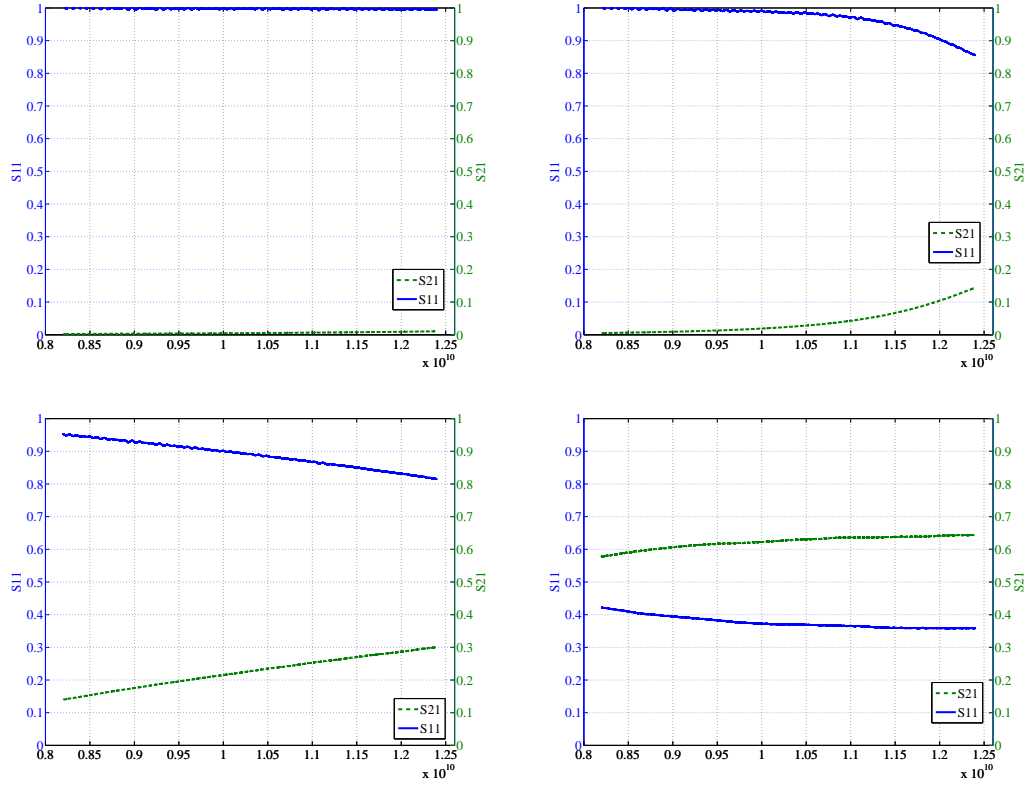


**Figure 28. Experimental scattering parameters for the 0.3 inch aperture flange (top-left: empty plate, top-right: filled plate, bottom-left: sheet, bottom-right: X-band).**

Without any apparent noise in the S21 parameters from the filled plate and sheet variants, it can be expected that root search technique would perform successfully for all cases. The extracted complex impedance from the empty plate flange, however, fails to converge to the correct values, as evidenced by Figures 29, 30, and 31. This is again due to insufficient energy coupling through the sample.

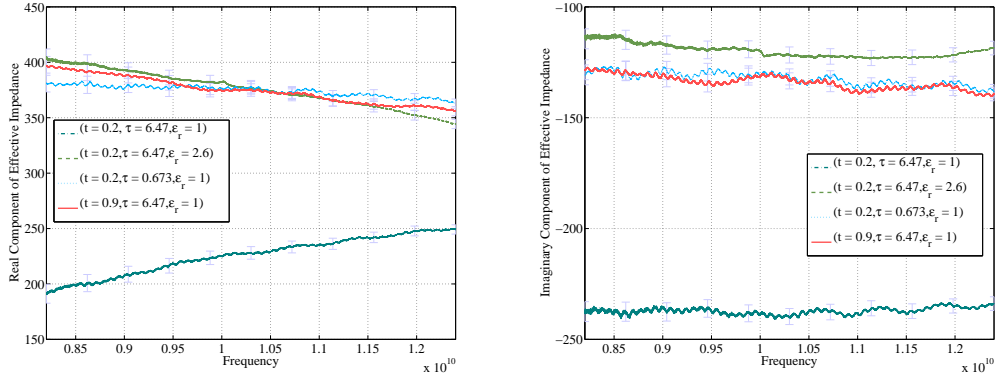


**Figure 29. Real and imaginary components of the effective impedance for the 400 ohm R-card with a 0.3 inch aperture flange.**

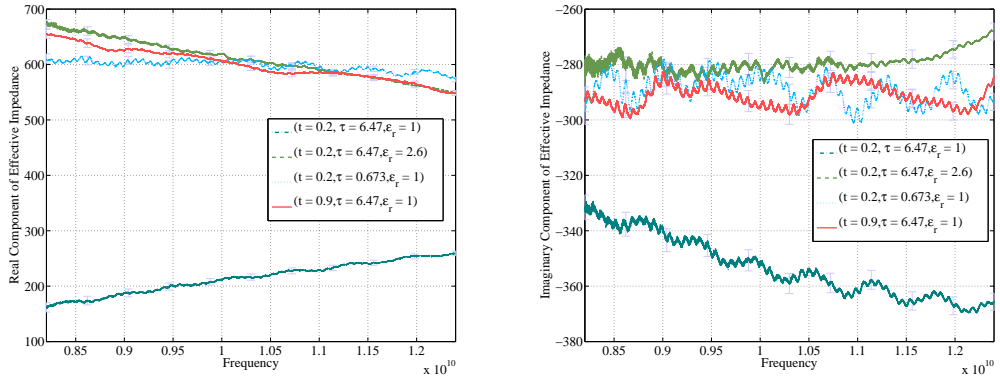


**Figure 30. Real and imaginary components of the effective impedance for the 900 ohm R-card with a 0.3 inch aperture flange.**

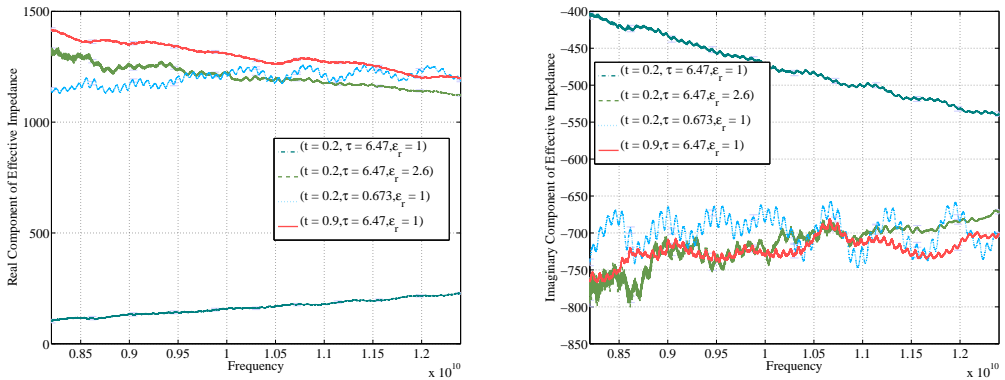


**Figure 31. Real and imaginary components of the effective impedance for the 2000 ohm R-card with a 0.3 inch aperture flange.**

A summary of the maximum difference between the 0.3 inch empty plate, filled plate, and sheet flange to the full X-band extracted complex impedance values is shown below.

**Table 5. Summary of Maximum Complex Impedance Error from the 0.3 inch Empty Plate Flange**

R-card	Real Component	Imaginary Component
400 $\Omega$	15.4%	75.2%
900 $\Omega$	51.2%	124.6%
2000 $\Omega$	167.9%	280.0%

**Table 6. Summary of Maximum Complex Impedance Error from the 0.3 inch Filled Plate Flange**

R-card	Real Component	Imaginary Component
400 $\Omega$	5.2%	4.6%
900 $\Omega$	3.2%	4.3%
2000 $\Omega$	8.7%	8.1%

**Table 7. Summary of Maximum Complex Impedance Error from the 0.3 inch Sheet Flange**

R-card	Real Component	Imaginary Component
400 $\Omega$	3.8%	1.9%
900 $\Omega$	6.8%	3.6%
2000 $\Omega$	19.6%	9.2%

For the empty plate flange S21 parameters, the inadequate amount of transmitted energy prohibits the root search technique from effectively extracting the correct complex permittivity values. The filled plate and sheet flange S21 parameters, with sufficient energy transmitted, produce very accurate complex permittivity values for each R-card sample. In each case where the complex impedance extraction algorithm failed, the experimentally measured S21 values fell near 0.1 or below. Thus, the experimental results collectively confirm a material measurement principle which requires that at least 10% of the incident electromagnetic energy be transmitted through the test sample for precision measurements.

#### 4.2.5 Summary.

While the Newton-Raphson root search is extremely accurate, it requires an initial guess of the unknown parameter. Without prior knowledge of the material under test the technique may not converge or could even converge to the incorrect solution. This problem is exacerbated when using relatively small scattering parameter measurements. With relatively small values the amount of uncertainty present has a more substantial effect on the root search algorithm, causing it to become unstable. Additionally, a minimum S21 measurement of 0.1 is required for precision electromagnetic characterization. Filling the stepped flange waveguide with a low loss dielectric, in this case plexiglass ( $\epsilon_r = 2.6$ ), allows about ten times as much incident energy to couple through the sample. Simply decreasing the thickness of the stepped flange, however, is more effective in permitting energy to couple through. The difference can be expected by considering the forward propagation component of the electromagnetic wave,

$$e^{-\gamma_m z} \quad \text{for } m = 1, \dots, M \quad (238)$$

$$\gamma_m = \sqrt{k_{xm}^2 - k^2}, \quad k = \frac{\omega}{c} \sqrt{\epsilon_r \mu_r}, \quad k_{xm} = (2m - 1) \frac{\pi}{t}, \quad (239)$$

where  $c$  is the speed of light,  $\epsilon_r$  is the relative permittivity of plexiglass,  $\mu_r$  is the relative permeability of plexiglass, and  $t$  is the thickness the waveguide width. Computing the amount of attenuation for the first  $m = 1, \dots, 10$  modes when passed through the plate and sheet flanges produces the following figures.

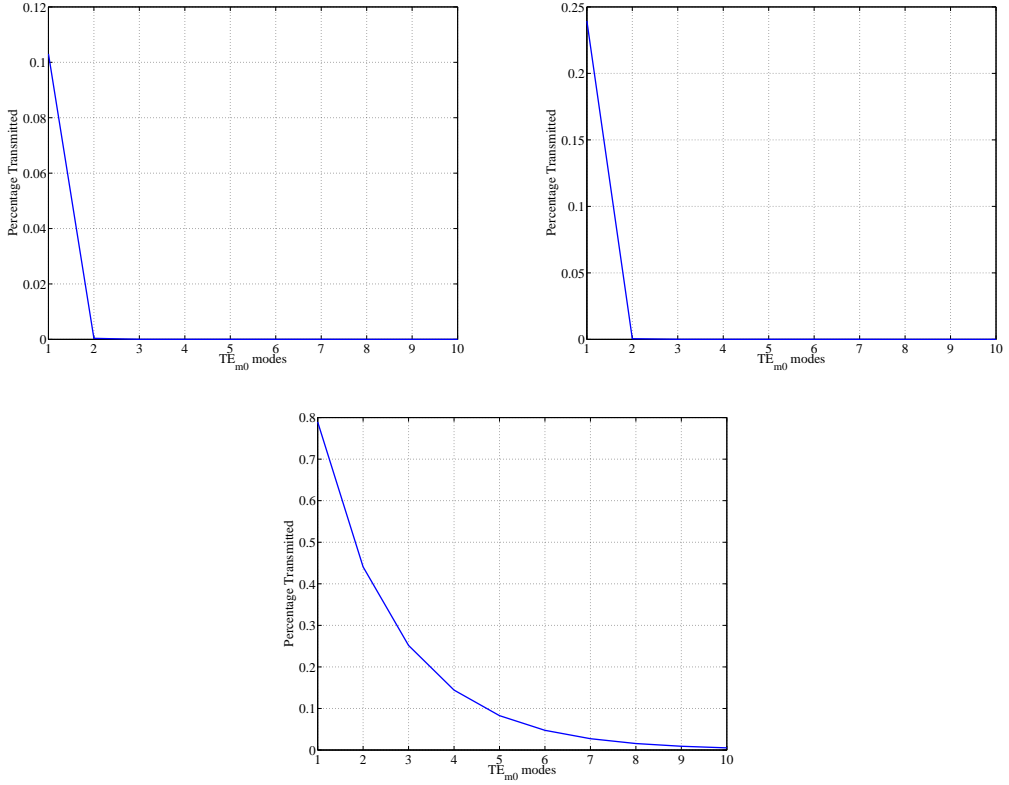


**Figure 32.** Percentage of first 10 modes to pass through the 0.3 inch stepped flange (top-left: empty plate flange, top-right: filled plate flange, bottom: sheet flange).

Analyzing Figure 32 confirms that simply decreasing the flange thickness more significantly increases the amount of electromagnetic energy coupled through the sample. For both the empty and filled flange cases, only the first two modes succeed in coupling through the sample, with the the second mode transmitting only at 0.04. Yet, the sheet flange effectively allow an appreciable amount of energy to be transmitted through nearly all ten modes.

## V. Conclusions and Recommendations

### 5.1 Conclusions

This research investigated the ability to simultaneously alter the real and imaginary components of an impedance sheet to achieve novel distributions for precision scattering and shielding control and manipulation. The theoretical development depended on an analytic approach for calculating the scattering characteristics from cylindrical sheet impedances having a  $\phi$  dependency with free-space filled, partially-filled PEC filled, and general dielectric filled cases. It relied on enforcement of general impedance sheet boundary conditions in addition to a Fourier series representation of the impedance sheet distribution with Wronskian and recurrence relations. For electromagnetic characterization, the additional degree of complexity caused by the  $\phi$  dependency was successfully mitigated in a piecewise homogeneous approach via a reduced aperture waveguide system. This stepped waveguide technique utilized a modal analysis to account for the excited higher-order modes, effectively allowing smaller cross-sections of the  $\phi$ -varying impedance sheet to be characterized. Furthermore, it was established that 10% of the incident electromagnetic energy at minimum must transmit through the sample under test to achieve precision electromagnetic characterization.

### 5.2 Future Research

For the novel impedance sheet distributions, advances in fabrication techniques will eventually allow larger tapered R-card samples to be made. Then, the scattering width 2D-to-3D conversion may be employed given that the minimum length criterion of 35 cm for X-band frequencies has been met and experimental testing may be completed. Another point of interest for the impedance sheet distributions is the idea

of multiple layers to possibly achieve less frequency dependence. This setup would required a layered Green's function analysis with the resistive sheet. Furthermore, it may be possible to achieve an analytic expression to relate both the position and reduction of effective nulls in the two-dimensional bistatic scattering width if the general approach is limited in scope to a single sinusoid. With the material characterization aspect, the presented reduced aperture waveguide system could possibly be improved upon by allowing the Vector Network Analyzer to average the experimental scattering parameters over 100 or more measurements. An additional material characterization technique that could be explored involves the tapered impedance sheet being rotated 180 degrees in a typical EMC/EMI setup while monostatic measurements are recorded for every increment of rotation. This method would require an adaptation of a method of moments approach to characterize the discretized tapered impedance sheet.

## Appendix A. Computationally-Efficient Formulation

The cylindrical wave transformation representation of the electromagnetic fields,  $\text{TM}^z$  and  $\text{TE}^z$ , can be written as

$$\vec{E}^i(\rho) = \hat{z}E_{0z}^i e^{-jzx} = \hat{z}E_{0z}^i \sum_{n=-\infty}^{\infty} j^{-n} J_n(k_0 \rho) e^{jn\phi}, \quad (240)$$

$$\vec{H}^i(\rho) = \hat{z}H_{0z}^i e^{-jzx} = \hat{z}H_{0z}^i \sum_{n=-\infty}^{\infty} j^{-n} J_n(k_0 \rho) e^{jn\phi}, \quad (241)$$

which can be manipulated into a more computationally efficient form through the use of certain Bessel function properties. Expanding the cylindrical wave function representation into three terms of negative indices, zero index, and positive indices results in

$$\sum_{n=-\infty}^{\infty} j^{-n} J_n(k_0 \rho) e^{jn\phi} = J_0(k_0 \rho) + \sum_{n=1}^{\infty} j^{-n} J_n(k_0 \rho) e^{jn\phi} + \sum_{n=-1}^{-\infty} j^{-n} J_n(k_0 \rho) e^{jn\phi}. \quad (242)$$

Re-indexing the last term for  $n \rightarrow -n$  produces

$$\sum_{n=-1}^{-\infty} j^{-n} J_n(k_0 \rho) e^{jn\phi} = \sum_{n=1}^{\infty} j^n J_{-n}(k_0 \rho) e^{-jn\phi} \quad (243)$$

$$= \sum_{n=1}^{\infty} j^n (-1)^n J_n(k_0 \rho) e^{-jn\phi} \quad (244)$$

$$= \sum_{n=1}^{\infty} (-j)^n J_n(k_0 \rho) e^{-jn\phi} \quad (245)$$

$$= \sum_{n=1}^{\infty} j^{-n} J_n(k_0 \rho) e^{-jn\phi}. \quad (246)$$

Substituting (246) back into (242)

$$\sum_{n=-\infty}^{\infty} j^{-n} J_n(k_0 \rho) e^{jn\phi} = J_0(k_0 \rho) + \sum_{n=1}^{\infty} j^{-n} J_n(k_0 \rho) (e^{jn\phi} + e^{-jn\phi}) \quad (247)$$

$$= J_0(k_0 \rho) + \sum_{n=1}^{\infty} j^{-n} J_n(k_0 \rho) (2 \cos n\phi) \quad (248)$$

$$= \sum_{n=0}^{\infty} \epsilon_n j^{-n} J_n(k_0 \rho) \cos n\phi, \quad (249)$$

where

$$\epsilon_n = \begin{cases} 1 & \dots n = 0 \\ 2 & \dots n \neq 0 \end{cases} . \quad (250)$$

The incident electromagnetic fields can now be represented in a more computationally efficient form as

$$\vec{E}^i(\vec{\rho}) = \hat{z} E_{0z}^i e^{-jkx} = \hat{z} E_{0z}^i \sum_{n=0}^{\infty} \epsilon_n j^{-n} J_n(k_0 \rho) \cos n\phi, \quad (251)$$

$$\vec{H}^i(\vec{\rho}) = \hat{z} H_{0z}^i e^{-jkx} = \hat{z} H_{0z}^i \sum_{n=0}^{\infty} \epsilon_n j^{-n} J_n(k_0 \rho) \cos n\phi. \quad (252)$$

## Appendix B. Wronskian and Recurrence Relations

Developed for the  $\text{TM}^z$  field set, the following will be additionally simplified by utilizing Wronskian and recurrence relations, such that

$$\begin{aligned} & J_n(k_0 a) H_n^{(2)'}(k_0 a) - J_n'(k_0 a) H_n^{(2)}(k_0 a) \\ &= J_n(k_0 a) [J_n'(k_0 a) - j Y_n'(k_0 a)] - J_n'(k_0 a) [J_n(k_0 a) - j Y_n(k_0 a)], \end{aligned} \quad (253)$$

$$= J_n(k_0 a) J_n'(k_0 a) - j J_n(k_0 a) Y_n'(k_0 a) - J_n'(k_0 a) J_n(k_0 a) + j J_n'(k_0 a) Y_n(k_0 a), \quad (254)$$

$$= j [J_n'(k_0 a) Y_n(k_0 a) - J_n(k_0 a) Y_n'(k_0 a)], \quad (255)$$

where Hankel functions of the second kind and their derivatives can be defined as

$$H_n^{(2)}(k_0 a) = J_n(k_0 a) - j Y_n(k_0 a), \quad (256)$$

$$H_n^{(2)'}(k_0 a) = J_n'(k_0 a) - j Y_n'(k_0 a). \quad (257)$$

Applying the following derivative Bessel function identity,

$$B_n'(z) = -B_{n+1}(z) + \frac{n}{z} B_n(z), \quad (258)$$

to (255) results in

$$\begin{aligned} J_n(k_0a)H_n^{(2)'}(k_0a) - J'_n(k_0a)H_n^{(2)}(k_0a) \\ = j \left[ \left( -J_{n+1}(k_0a) + \frac{n}{k_0a} J_n(k_0a) \right) Y_n(k_0a) \right. \\ \left. - J_n(k_0a) \left( -Y_{n+1}(k_0a) + \frac{n}{k_0a} Y_n(k_0a) \right) \right], \end{aligned} \quad (259)$$

$$\begin{aligned} = j \left[ -J_{n+1}(k_0a)Y_n(k_0a) + \frac{n}{k_0a} J_n(k_0a)Y_n(k_0a) \right. \\ \left. + J_n(k_0a)Y_{n+1}(k_0a) + \frac{n}{k_0a} J_n(k_0a)Y_n(k_0a) \right], \end{aligned} \quad (260)$$

$$= j [J_n(k_0a)Y_{n+1}(k_0a) - J_{n+1}(k_0a)Y_n(k_0a)], \quad (261)$$

$$= j(-1) \frac{2}{\pi k_0 a}. \quad (262)$$

Thus, utilizing both Wronskian and recurrence relations leads ultimately to the following relation

$$J_n(k_0a)H_n^{(2)'}(k_0a) - J'_n(k_0a)H_n^{(2)}(k_0a) = -\frac{j2}{\pi k_0 a}. \quad (263)$$

Developed for the  $TE^z$  field set, the following will be additionally simplified by utilizing Wronskian and recurrence relations, where

$$\begin{aligned} J'_n(k_0a)H_n^{(2)}(k_0a) - J_n(k_0a)H_n^{(2)'}(k_0a) \\ = J'_n(k_0a) [J_n(k_0a) - jY_n(k_0a)] - J_n(k_0a) [J'_n(k_0a) - jY'_n(k_0a)], \end{aligned} \quad (264)$$

$$= J'_n(k_0a)J_n(k_0a) - jJ'_n(k_0a)Y_n(k_0a) - J_n(k_0a)J'_n(k_0a) + jJ_n(k_0a)Y'_n(k_0a), \quad (265)$$

$$= j [J_n(k_0a)Y'_n(k_0a) - J'_n(k_0a)Y_n(k_0a)], \quad (266)$$

where Hankel functions of the second kind and their derivatives can be defined as

$$H_n^{(2)}(k_0a) = J_n(k_0a) - jY_n(k_0a), \quad (267)$$

$$H_n^{(2)'}(k_0a) = J_n'(k_0a) - jY_n'(k_0a). \quad (268)$$

Applying the following derivative Bessel function identity,

$$B_n'(z) = -B_{n+1}(z) + \frac{n}{z}B_n(z), \quad (269)$$

to (266) results in

$$\begin{aligned} & J_n'(k_0a)H_n^{(2)}(k_0a) - J_n(k_0a)H_n^{(2)'}(k_0a) \\ &= j \left[ J_n(k_0a) \left( -Y_{n+1}(k_0a) + \frac{n}{k_0a}Y_n(k_0a) \right) \right. \\ & \quad \left. - \left( -J_{n+1}(k_0a) + \frac{n}{k_0a}J_n(k_0a) \right) Y_n(k_0a) \right], \end{aligned} \quad (270)$$

$$\begin{aligned} &= j \left[ -J_n(k_0a)Y_{n+1}(k_0a) + \frac{n}{k_0a}J_n(k_0a)Y_n(k_0a) \right. \\ & \quad \left. + J_{n+1}(k_0a)Y_n(k_0a) - \frac{n}{k_0a}J_n(k_0a)Y_n(k_0a) \right], \end{aligned} \quad (271)$$

$$= j [J_{n+1}(k_0a)Y_n(k_0a) - J_n(k_0a)Y_{n+1}(k_0a)], \quad (272)$$

$$= j \frac{2}{\pi k_0 a}. \quad (273)$$

Thus, utilizing both Wronskian and recurrence relations leads ultimately to the following relation

$$J_n'(k_0a)H_n^{(2)}(k_0a) - J_n(k_0a)H_n^{(2)'}(k_0a) = \frac{j^2}{\pi k_0 a}. \quad (274)$$

## Bibliography

- [1] M. Ramdani, E. Sicard, A. Boyer, S. Ben Dhia, J.J. Whalen, T.H. Hubing, M. Coenen, and O. Wada. The electromagnetic compatibility of integrated circuits—past, present, and future. *Electromagnetic Compatibility, IEEE Transactions on*, 51(1):78–100, Feb. 2009.
- [2] B. Glover, K. Whites, M. Hyde, and M. Havrilla. Complex effective permittivity of carbon loaded dielectric films with printed metallic square rings. *Proc. Metamaterials*, pages pp. 762–764, September 2008.
- [3] M.W. Hyde, M.J. Havrilla, and P.E. Crittenden. A novel method for determining the r-card sheet impedance using the transmission coefficient measured in free-space or waveguide systems. *Instrumentation and Measurement, IEEE Transactions on*, 58(7):2228–2233, July 2009.
- [4] J. Lee, M. Havrilla, M. Hyde, and E.J. Rothwell. Scattering from a cylindrical resistive sheet using a modified physical optics current. *Microwaves, Antennas and Propagation, IET*, 2(5):482–491, August 2008.
- [5] B. Thomas. Scattering by resistive strips. *Radio Sci.*, vol. 14(no. 5):pp. 911–924, 1979.
- [6] K. Barkeshli and J.L. Volakis. Electromagnetic scattering from thin strips. i. analytical solutions for wide and narrow strips. *Education, IEEE Transactions on*, 47(1):100–106, Feb. 2004.
- [7] K. Barkeshli and J.L. Volakis. Electromagnetic scattering from thin strips. ii. numerical solution for strips of arbitrary size. *Education, IEEE Transactions on*, 47(1):107–113, Feb. 2004.
- [8] K. Sarabandi. Scattering from variable resistive and impedance sheets. *J. Electromagn. Waves Applicat.*, vol. 4(no. 9):pp. 865–891, 1990.
- [9] Z. Sipus, R. Zentner, and J. Bartolic. Validity of approximate boundary conditions for periodic strips on cylindrical substrates. In *Mathematical Methods in Electromagnetic Theory*, volume 1, pages 171–173 vol.1, Jun 1998.
- [10] T.B.A. Senior and J.L. Volakis. Generalized impedance boundary conditions in scattering. *Proceedings of the IEEE*, 79(10):1413–1420, Oct 1991.
- [11] A. Karlsson. Approximate boundary conditions for thin structures. *Antennas and Propagation, IEEE Transactions on*, 57(1):144–148, Jan. 2009.
- [12] R. Haupt and V. Liepa. Synthesis of tapered resistive strips. *Antennas and Propagation, IEEE Transactions on*, 35(11):1217–1225, Nov 1987.

- [13] R.L. Haupt and V.V. Liepa. Resistive tapers that place nulls in the scattering patterns of strips. *Antennas and Propagation, IEEE Transactions on*, 38(7):1117–1119, Jul 1990.
- [14] Sean P. Dorey. Stepped waveguide electromagnetic material characterization technique. Master’s thesis, Air Force Institute of Technology, 2004.
- [15] Milo W. Hyde. Determining the resistivity of resistive sheets using transmission measurements. Master’s thesis, Air Force Institute of Technology, 2006.
- [16] Constantine A. Balanis. *Advanced Engineering Electromagnetics*. John Wiley and Sons, 1989.
- [17] J. G. V. Bladel. *Electromagnetic Fields*. John Wiley and Sons, 2007.
- [18] R. E. Collin. *Field Theory of Guided Waves*. John Wiley and Sons, 1991.
- [19] R. F. Harrington. *Time-Harmonic Electromagnetic Fields*. John Wiley and Sons, 2001.
- [20] Peterson, A. F. Ray, and R. S. L. Mittra. *Computational Methods for Electromagnetics*. John Wiley and Sons, 1998.
- [21] J. A. Stratton. *Electromagnetic Theory*. John Wiley and Sons, 2006.
- [22] Vanzura E.J. Kissick W.A. Baker-Jarvis, J. Improved technique for determining complex permittivity with the transmission/reflection method. *Microwave Theory and Techniques, IEEE Transactions on*, 38(8):1096 –1103, Aug. 1990.

REPORT DOCUMENTATION PAGE				Form Approved OMB No. 074-0188
<p>The public reporting burden for this collection of information is estimated to average 1 hour per response, including the time for reviewing instructions, searching existing data sources, gathering and maintaining the data needed, and completing and reviewing the collection of information. Send comments regarding this burden estimate or any other aspect of the collection of information, including suggestions for reducing this burden to Department of Defense, Washington Headquarters Services, Directorate for Information Operations and Reports (0704-0188), 1215 Jefferson Davis Highway, Suite 1204, Arlington, VA 22202-4302. Respondents should be aware that notwithstanding any other provision of law, no person shall be subject to an penalty for failing to comply with a collection of information if it does not display a currently valid OMB control number.</p> <p><b>PLEASE DO NOT RETURN YOUR FORM TO THE ABOVE ADDRESS.</b></p>				
1. REPORT DATE (DD-MM-YYYY) 25-03-2010	2. REPORT TYPE Thesis	3. DATES COVERED (From – To) Sep 2008 – Mar 2010		
<p><b>4. TITLE AND SUBTITLE</b>  ARTIFICIAL INHOMOGENEOUS TAPERED IMPEDANCE SHEET CHARACTERIZATION AND APPLICATIONS</p>		5a. CONTRACT NUMBER		
		5b. GRANT NUMBER		
		5c. PROGRAM ELEMENT NUMBER		
<p><b>6. AUTHOR(S)</b>  Massman, Jeffrey P., 2d Lt, USAF</p>		5d. PROJECT NUMBER 2007-124		
		5e. TASK NUMBER		
		5f. WORK UNIT NUMBER		
<p><b>7. PERFORMING ORGANIZATION NAMES(S) AND ADDRESS(S)</b> Air Force Institute of Technology Graduate School of Engineering and Management 2950 Hobson Way, WPAFB, OH 45433</p>			8. PERFORMING ORGANIZATION REPORT NUMBER AFIT/GE/ENG/10-16	
<p><b>9. SPONSORING/MONITORING AGENCY NAME(S) AND ADDRESS(ES)</b> Air Force Research Laboratory Sensors Directorate Attn: Mr. Garrett Stenholm 2591 K Street, Bldg. 254 Wright-Patterson AFB, OH 45433-7602 (937) 255-9179 Garrett.Stenholm@wpafb.af.mil</p>			<p>10. SPONSOR/MONITOR'S ACRONYM(S) AFRL/RYS</p> <p>11. SPONSOR/MONITOR'S REPORT NUMBER(S)</p>	
<p><b>12. DISTRIBUTION/AVAILABILITY STATEMENT</b>  Approval for public release; distribution is unlimited</p>				
<p><b>13. SUPPLEMENTARY NOTES</b></p>				
<p><b>14. ABSTRACT</b> The ability to manipulate a complex impedance sheet about a PEC or general dielectric cylinder of arbitrary diameter to control the overall scattering characteristics at particular angles for shielding or scattering applications is presented. It is shown that with the capability to readily control both the real and imaginary components of a percolated lossy film's effective impedance, specific impedance distributions can be obtained to effectively direct the overall nulls in the bistatic scattering pattern. The exact approach only requires negligible truncation error of the matrix solution and can be applied to cylinders of arbitrary size. This approach relies on general impedance sheet boundary conditions in addition to a Fourier series representation of the impedance sheet distribution, with the utilization of Wronskian and recurrence relations, to produce a computationally efficient matrix solution for the scattered field expansion coefficient <math>a_n</math>. This scattering coefficient <math>a_n</math> can then be included in the expression for a two-dimensional scattering width, allowing for the computation of scattering patterns of arbitrary diameter cylinder impedance sheet distributions. The ability to adapt sheet impedances to effectively control the overall nulls in the bistatic scattering pattern will be demonstrated, with practically-implemented impedance characteristics. Lastly, a novel rectangular X-band waveguide system will be utilized to characterize the electromagnetic properties of the phi-dependent impedance sheet.</p>				
<p><b>15. SUBJECT TERMS</b> Impedance Sheet, R-card, EMC/EMI, Scattering</p>				
<p><b>16. SECURITY CLASSIFICATION OF:</b></p>		<p><b>17. LIMITATION OF ABSTRACT</b></p>	<p><b>18. NUMBER OF PAGES</b></p>	<p><b>19a. NAME OF RESPONSIBLE PERSON</b> Michael J. Havrilla</p> <p><b>19b. TELEPHONE NUMBER</b> (Include area code) <a href="mailto:michael.havrilla@afit.edu">michael.havrilla@afit.edu</a> 937-255-3636 x4582</p>
REPORT U	ABSTRACT U	c. THIS PAGE U	UU	89

Standard Form 298 (Rev: 8-98)

Prescribed by ANSI Std Z39-18